Chapter 06: Ball-Milling and Spark-Plasma Sintering of Alloys

6.1 Introduction

Fe-based BMG materials are perhaps the most important system for structural applications because of their high strength and hardness[218], [219]. A few studies were conducted using the powder metallurgy (PM) route for Fe-based powders. Fe-based powders prone to glass formation are usually used in thermal spraying[220], [221], Spark plasma sintering (SPS)[49], [222], [223] or 3-D printing[224], [225] to prepare the coating. SPS seems to be preferred for the fabrication of novel amorphous/ nanocrystalline materials[56]. This process provides sintered product in shorter processing times without altering microstructures. The combined advantage of PM with SPS has been discussed in chapter-3.

The amorphous phase can be formed by high energy ball milling process [226]. Schultz[227] has produced Fe-Zr-B amorphous alloy powders by this technique and found that elemental boron was difficult to react completely with other constituents and a post heat treatment was required to promote the diffusion of boron into the amorphous matrix. Sunol et al.[219], reported Fe-Ni-P-Si amorphous alloys and concluded that using Fe and Ni reduced the energy of formation of the amorphous phase and the time necessary to produce this phase during the MA Process. Schlorke et al.[228], reported the amorphous phase formation in the Fe-Al-Ga-P-C-B system after 130h of mechanical alloying. Murty et al.[229], produced bulk amorphous alloy in Fe-Cr-Mo-P-B-C-Si system by MA followed by SPS technique. Singh and Harimkar[222], reported Fe-Cr-Mo-C-B-Y system-based amorphous matrix composites by the SPS process. To enhance the plasticity of structural amorphous materials, they reinforced the tungsten particles into the amorphous matrix.

This chapter deals with the synthesis of four Fe-based nanocrystalline/composites by mechanical milling followed by spark-plasma-sintering technique from the alloys that are produced by Cu-mould casting as discussed in Chapter 4. The nominal compositions of these composites are given in the experimental section of this chapter. The microstructure or phase evolution in the ball-milling process as well as after SPS of the compact are presented. The micro-indentation behavior of 100h of ball-milled consolidated powders will be reported. The load-dependent hardness behavior and yield strength of sintered pellets are ascertained experimentally. The fracture toughness of consolidated samples is estimated through the propagation of cracks during indentation.

6.2 Experimental Procedure

A high-energy planetary ball mill (Retsch, PM400/2) was used for the synthesis of four different alloy powders having nominal compositions of $Fe_{56.24}Cr_4Mo_{14}C_{15}Si_{3.8}B_6$, $Fe_{43.47}Cr_{15}Mo_{14}C_{15.12}Si_{3.78}B_6Y_2$, $Fe_{40.2}Cr_{20}Mo_{10}W_2C_{15}Si_{4.2}B_6Y_2$ and $Fe_{40.2}Cr_{15}Mo_{14}Co_3C_{15}Si4.2B_6Y_2$. The 10g of each alloy produced by Cu-mould casting as discussed in Chapter 4, were taken and crushed into small granules in order of ~1mm and washed in ethanol, and dried. The ratio of weights of ball to powder was taken at 10:1. The milling was carried out in tungsten carbide (WC) vials with tungsten carbide balls (~6mm diameter). To avoid oxidation and heating effects, toluene was used as a process control reagent. The milling operation was stopped intermittently for 30 minutes for every 1h of milling. The alloys were milled for up to 100h duration. The designations of ball-milled powders are BMP-A, BMP-B, BMP-C, and BMP-D respectively. Further the 100h milled powder of each composition was compacted by spark plasma sintering technique (SPS1000: Suga Co.Ltd., Japan) at a temperature of 800^oC, pressure 50MPa, and heating rate of 100 ^oC/min with a holding time of 15min. A 10mm diameter and 5mm thick disc were produced by the SPS technique as shown in Fig. 6.1.

The Archimedes principle was used to measure the bulk densities of SPSed samples (model no. CAH-503, CONTECH instrumented Ltd. Mumbai). The density of SPSed samples is given in Table 6.1.

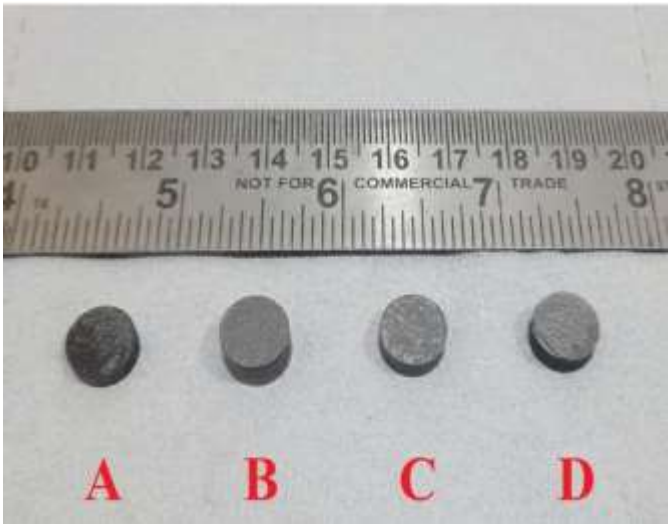

Fig. 6. 1: Optical image of SPSed samples with 10mm diameter disc

The microstructures of sintered samples were observed under an optical microscope (OM) (Leica model LV 500). The required size of alloys was taken for metallographic examination by following standard procedures for specimen preparation. The morphology of these samples was studied by scanning electron microscope (SEM) (Model: FEI Quanta 200F) operated at 30KV and equipped with an EDS detector. The investigation of structure and phases evolve in ball-milled powders was carried out X-ray diffraction (MiniFlex600, RIGAKU) instrument using a Cu-K_α (λ~1.54A^o) radiation source. The operating voltage and current were kept at 40kV and 15mA respectively. For the sintered alloys, we have used an X-ray diffractometer (HR-XRD EMPYREAN, PANALYTICAL) with Co-K_α (λ~1.78A^o) source, with 40 kV and 40mA operating voltage and current respectively. All the samples are cut in the required shape and put on the sample holder. All the samples were scanned from 2θ=20 to 100^o angle. The interpretation of X-ray diffraction patterns was finalized with the help of standard JCPDS/ICDD data cards. The indentation characteristics are measured by an instrumented micro-hardness tester (Anton Parr: MHT^3). A Vickers diamond indenter was used. I have applied the indentation load from 10mN to up to fracture of the specimen with 20 sec of dwell time. At least ten indentations were done at each of the loads for reproducibility.

6.3 Results

6.3.1 Density Measurement

The Archimedes principle was used for the measurement of the density of sintered samples. This experiment was repeated four times to report the average value. The measured values of the density of these alloys are given in Table 6.1.

Table 6. 1: The bulk (experimental) density of Sintered composite

Sintered Alloys	**Compositions (at. %)**	**Bulk Density(g/cc)**
SPSed-A	$Fe_{56.24}Cr_4Mo_{14}C_{15}Si_{3.8}B_6$	5.02
SPSed-B	$Fe_{43.47}Cr_{15}Mo_{14}C_{15.12}Si_{3.78}B_6Y_2$	7.66
SPSed-C	$Fe_{40.2}Cr_{20}Mo_{10}W_2C_{15}Si_{4.2}B_6Y_2$	7.62
SPSed-D	$Fe_{40.2}Cr_{15}Mo_{14}Co_3C_{15}Si4_{.2}B_6Y_2$	6.28

6.3.2 Evolution of Microstructures

Figures 6.2 (a-d) and fig. 6.3 (a-d) gives the optical and SEM micrographs of sintered samples of SPSed-A, SPSed-B, SPSed-C, and SPSed-D. The micrographs of sintered samples show that all the samples possess uniform microstructure and are well sintered, except the sample of SPSed-A, shown in Fig. 6.2(a) and Fig. 6.3 (a). All the samples were compacted by SPS at the same temperature (~ 800 ^{o}C) and under similar operating conditions. The density of SPSed-A is poor (~5g/cc). It is due to the formation of porosity in the sample. This was seen in optical as well as SEM micrographs of SPSed-A. The arrow marks shown in Fig. 6.3 (b and c) represent some foreign particles embedded in the matrix. These particles could either be oxides or tungsten. I have used WC vials and balls therefore there may be a chance of a little contamination of W from WC vials and balls after a long time of milling. It will be confirmed after the EDS analysis of these samples in the next sub-sections 6.3.5 and 6.3.6.

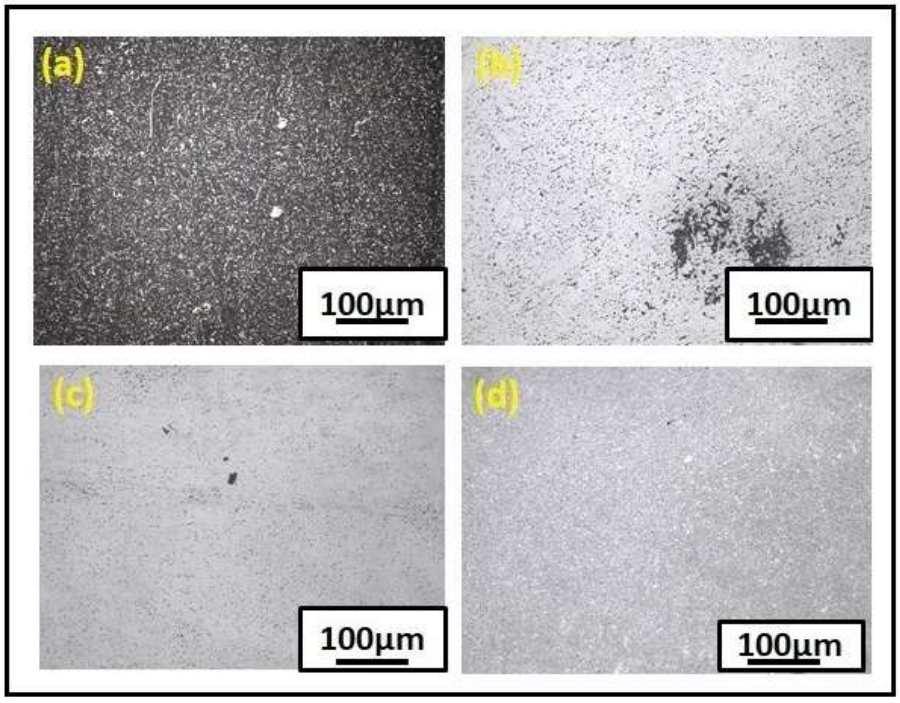

Fig. 6. 2: Showing optical micrographs of 100h ball milled powders of sintered samples (a) SPSed-A, (b) SPSed-B, (c) SPSed-C, and (d) SPSed-D, sintered at 800 ^{o}C.

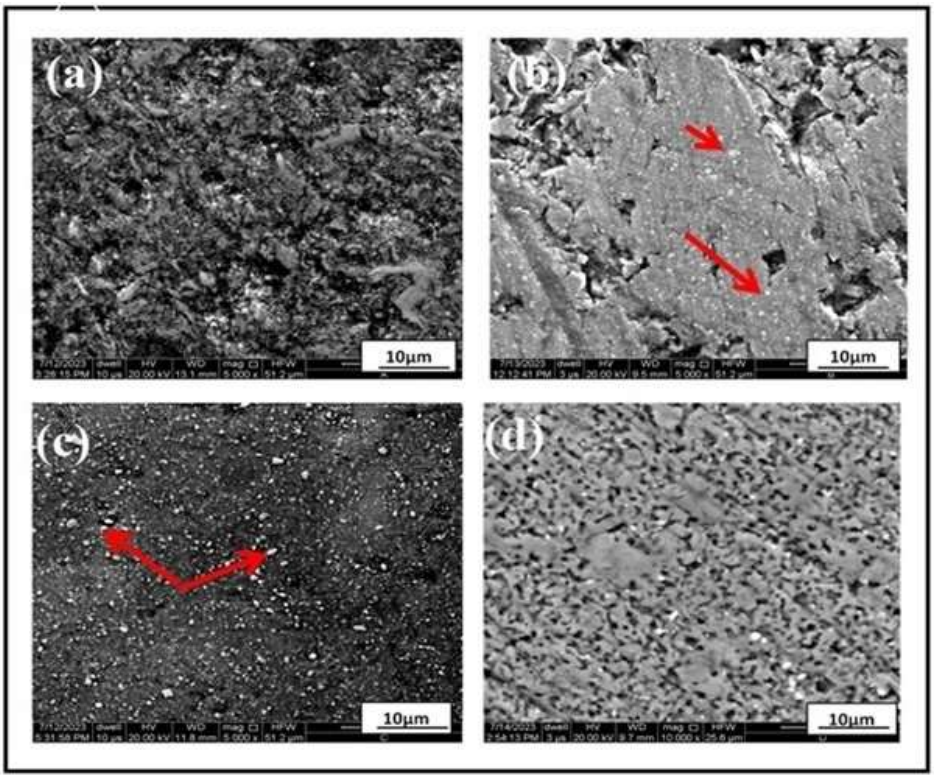

Fig. 6. 3: Showing SEM images of 100h ball milled powders of sintered samples (a) SPSed-A, (b) SPSed-B, (c) SPSed-C, and (d) SPSed-D, sintered at 800 ^{o}C.

6.3.3 X-ray Diffraction Analysis of Ball milled Powder

The X-ray diffraction patterns of ball-milled sample BMP-A ($Fe_{56.24}Cr_4Mo_{14}C_{15}Si_{3.8}B_6$) with different milling times are presented in Fig. 6.4. The XRD patterns at 0h of milling showing XRD patterns of Cu-mould cast alloys, as I have chosen these alloys for making powders through the ball-milling process. The alloy processed through Cu-mould casting shows multiple crystalline phases of $Fe_{11}Mo_6C_5$ (mC44), Fe_5C_2 (mC28), Cr_7C_3 (oP40), and α-Fe (cI2) already discussed in Chapter 4. In the case of the XRD patterns of ball-milled powders with milling hours, some broad and less intense crystalline peaks are observed in the same 2θ range as observed in the as-cast alloy. As milling progresses the intensity of peaks gets reduced and peak broadening appears along with the disappearance of some of the phases. It has been also observed that the carbides of Fe_5C_2 and Cr_7C_3 phases have completely disappeared after 30h and 70h of milling respectively. The phases corresponding to the most intense peaks in as-cast alloys are also present throughout the milling. I have milled the powders up to 120h and observed no further changes in phases evolved after 100h of milling. Hence, XRD patterns up to 100h of milling will now be presented and discussed.

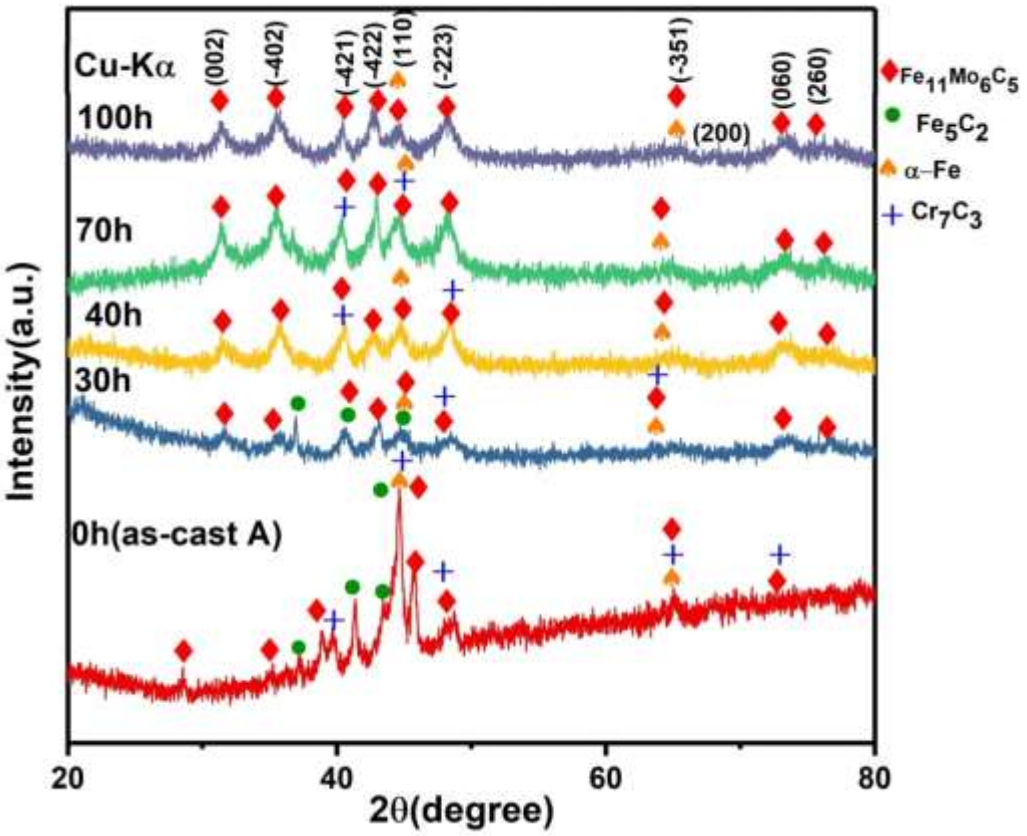

Fig. 6. 4: X-ray diffraction patterns of ball-milled sample BMP-A ($Fe_{56.24}Cr_4Mo_{14}C_{15}Si_{3.8}B_6$), at various milling time

Figure 6.5 represents the X-ray diffraction patterns with milling hours of the BMP-B sample having a nominal composition of $Fe_{43.47}Cr_{15}Mo_{14}C_{15.12}Si_{3.78}B_6Y_2$. It was observed that the phase Fe_3W_3C that evolved in 0 hours of milling (i.e., in as-cast alloy-B) completely disappeared after 10 hours of milling. The number of peaks corresponding to the Cr_7C_3 phase is predominantly present. However, at the end of 100h of milling the phase of Cr_7C_3 is completely absent. At the end of milling, only two phases remain in the XRD pattern, these are α-Fe and $Fe_{11}Mo_6C_5$. In the XRD pattern of BMP-C, as shown in Fig. 6.6, it has been observed that Fe_3C and Cr_7C_3 phases evolved in as-cast alloy-C and remain in the powder for up to 60 hours of milling. As milling progresses these phases are completely dissolved and at the end of 100h milling, only two phases are seen. Similar kinds of observations can be made based on XRD patterns of BMP-D as shown in Fig. 6.7. In addition to this, it was noticed that XRD patterns of BMP-C and BMP-D after 60h of milling give rise to the formation of a new phase. It indicates that a phase transformation has taken. This could be one of the reasons by which faceted morphology was observed in BMP-C and BMP-D (cf. fig. 6.14 (C) and (D)). It is worth pointing out that, at the end of milling (~100h milling time) two phases are observed in each composition. These phases are α-ferrite and

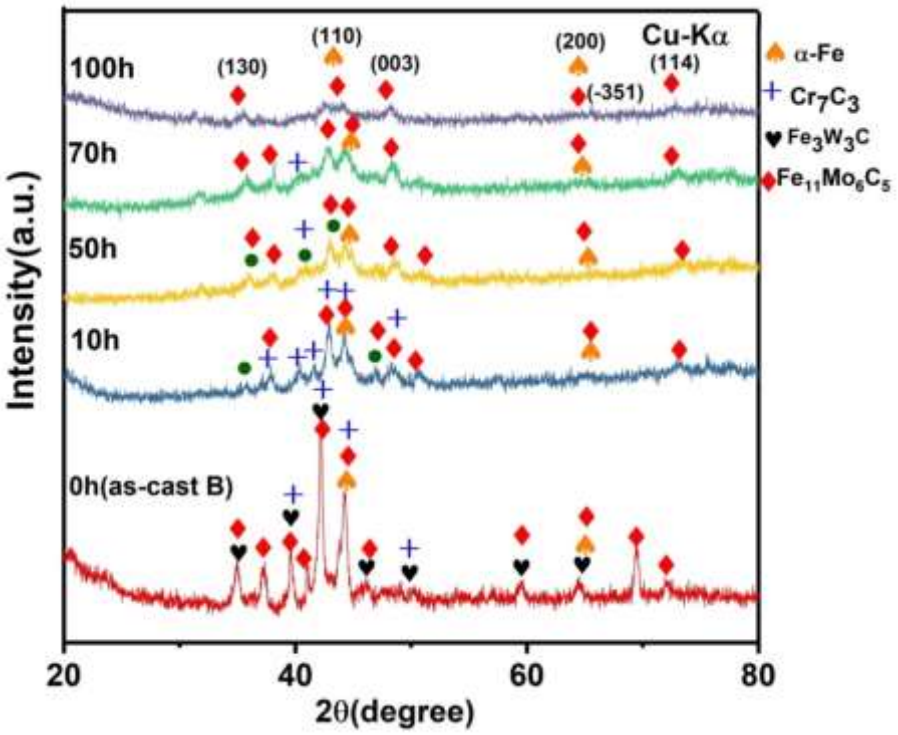

Fig. 6. 5: X-ray diffraction patterns of ball-milled BMP-B ($Fe_{43.47}Cr_{15}Mo_{14}C_{15.12}Si_{3.78}B_6Y_2$) sample, at various milling time

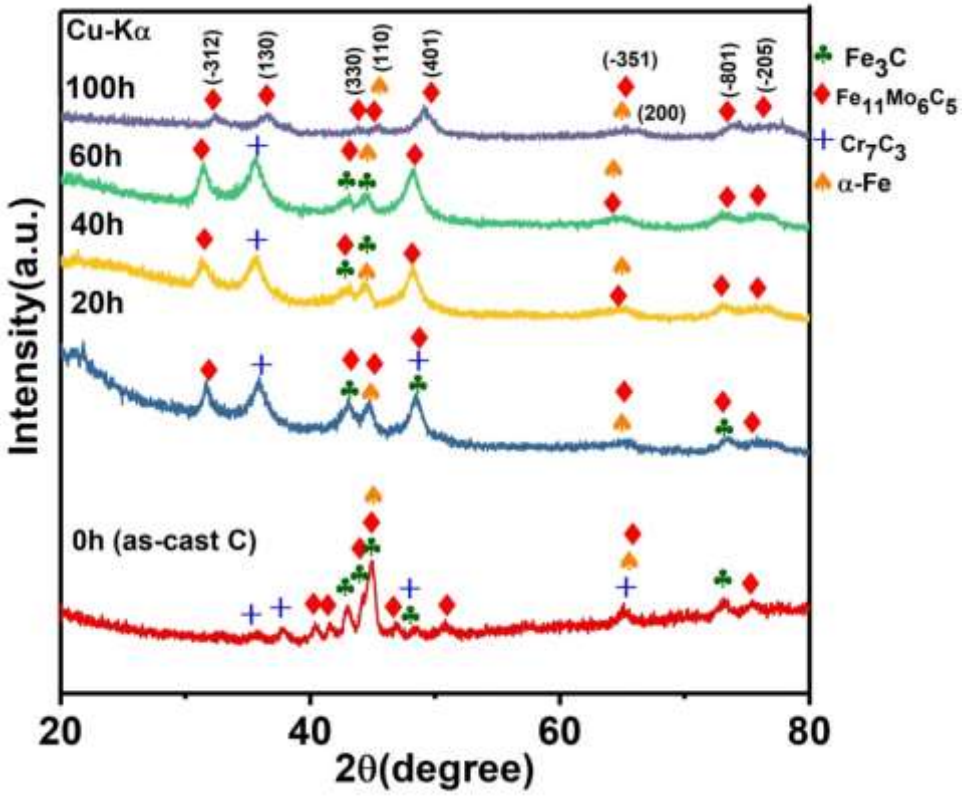

Fig. 6. 6: X-ray diffraction patterns of ball-milled BMP-C ($Fe_{40.2}Cr_{20}Mo_{10}W_2C_{15}Si_{4.2}B_6Y_2$) sample, at various milling time

$Fe_{11}Mo_6C_5$. They show relative stability under milling for longer hours.

The average crystallite size (nm) and microstrain (%) of ball-milled powder of composite A, B, C, and D were calculated by using the Williamson-Hall method, as described in sub-section 3.4.3 of Chapter 3. The variation of crystallite and micro-strain of ball-milled powders (BMPs) are shown in Fig.6.8. It was found that the crystallite size of BMP-A continuously decreases with milling time and micro-strain increases as shown in Fig. 6.8 (a). At the end of milling the crystallite size and micro-strain of BMP-A are ~8nm and ~1.2% strain obtained in BMP-B (fig.6.8 (b)).

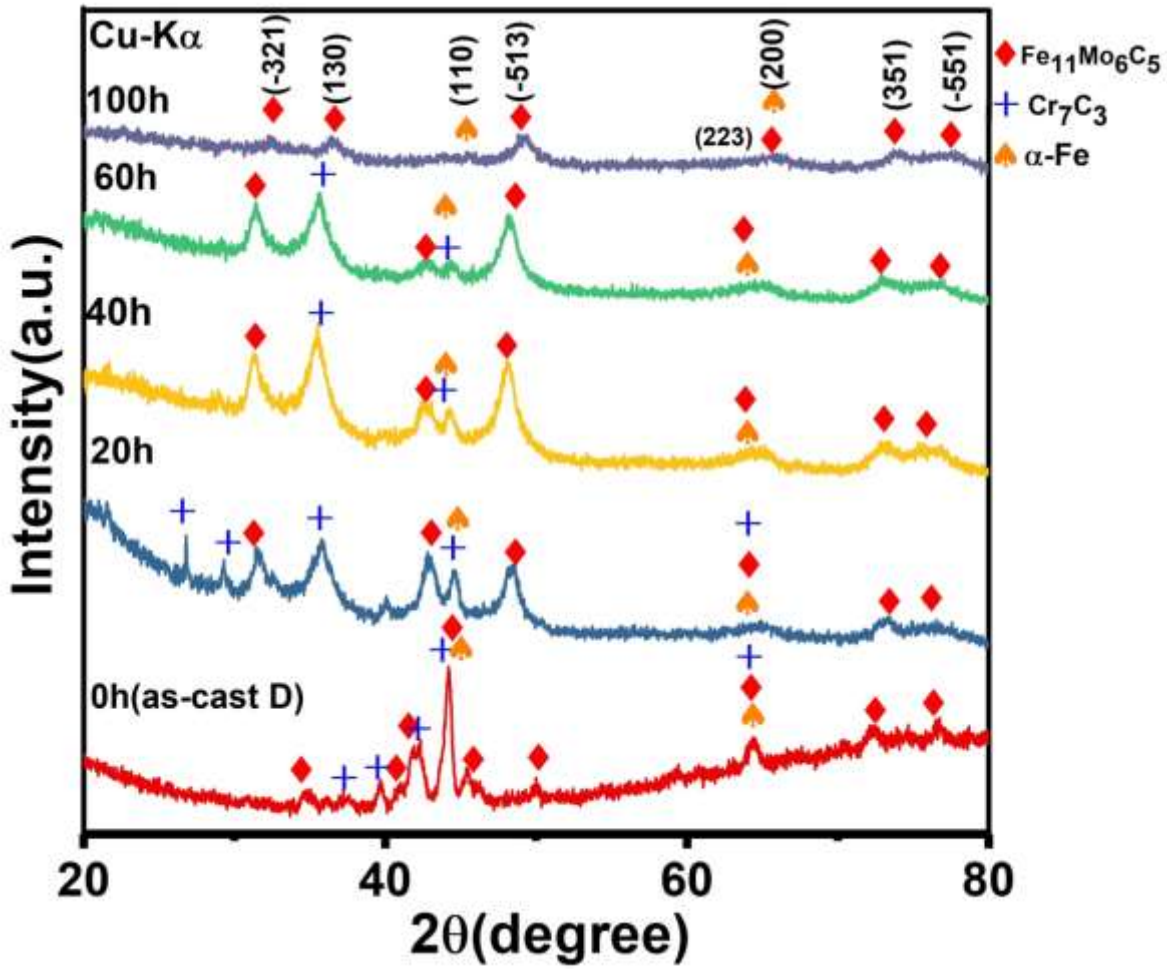

Fig. 6. 7: X-ray diffraction patterns of ball-milled BMP-D ($Fe_{40.2}Cr_{15}Mo_{14}Co_3C_{15}Si4.2B_6Y_2$) sample, at various milling time

The crystallite size and micro-strain vary in irregular ways with milling time in all ball-milled powders (except BMP-A) during the mechanical milling process. The average crystallite size observed at the end of milling in BMP-D (fig. 6.8(d)) i.e. ~8nm and minimum average micro-

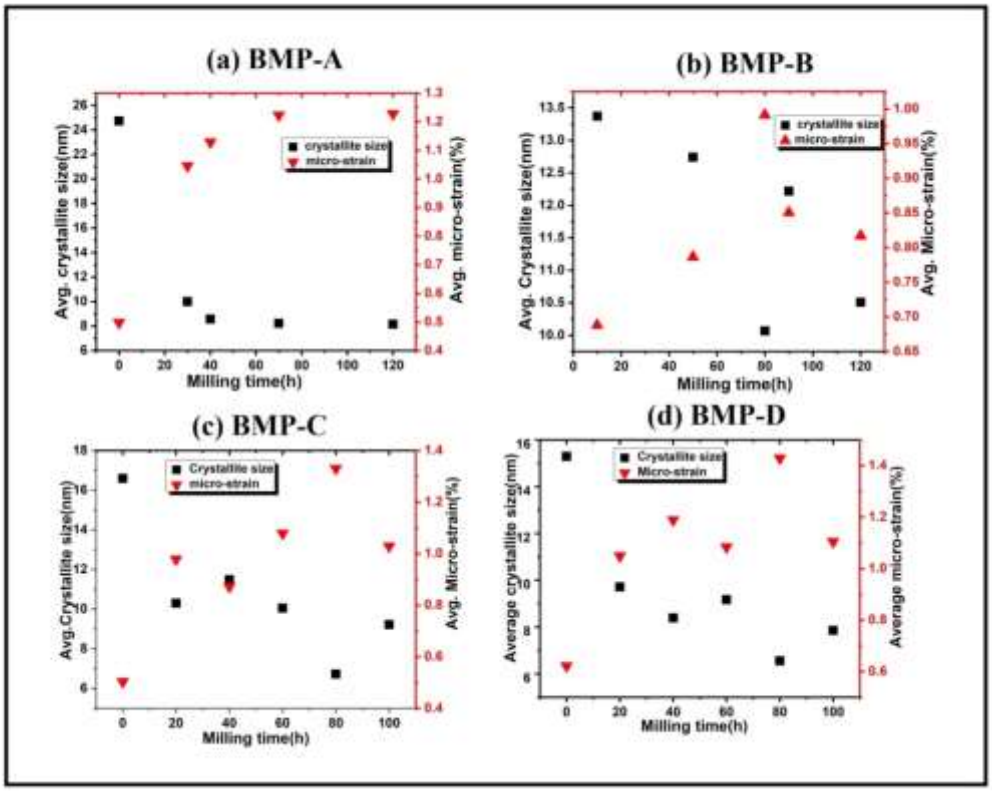

Fig. 6. 8: Variation of average crystallite-size and micro-strain with milling time of ball-milled powders (a) BMP-A, (b) BMP-B, (c) BMP-C, and (d) BMP-D

Table 6. 2: Variation of average crystallite size and micro-strain with milling time in ball-milled nanocomposite powder

	BMP-A		**BMP-B**		**BMP-C**		**BMP-D**	
Milling time(h)	**ACS (nm)**	**AMS (%)**	**ACS (nm)**	**AMS (%)**	**ACS (nm)**	**AMS (%)**	**ACS (nm)**	**AMS (%)**
10	-	-	13	0.75	-	-	-	-
20	-	-	-	-	10	0.95	9.5	1.05
30	10	1.04	-	-	-	-	-	-
40	8.5	1.13	-	-	11	0.85	8	1.18
50	-	-	12.5	0.8	-	-	-	-
60	-	-	-	-	10	1.05	9	1.08

70	8	1.22	-	-	-	-	-	-
80	-	-	10	0.9	6.5	1.33	6.5	1.42
100	8	1.22	10	0.85	9	1.02	7.5	1.10
ACS-Average crystallite size; AMS-Average micro-strain								

corresponding to it. The variation in crystallite size may be due to the formation of new phases in BMP-A, BMP-B, and BMP-C. The variation of average crystallite size (in nm) and average microstrain (in %) with milling in the entire ball-milled nanocomposite powders are given in Table 6.2.

6.3.4 X-ray Diffraction Analysis of SPSed alloys

The 100h ball milled nanocomposite powder was consolidated by SPS at 800^{o}C (1073K) for 15 minutes with a pressure of 50 MPa. The phase evolutions and phase transformation in 100h ball-milled powders and corresponding sintered alloys are shown in this sub-section. Figures 6.9 (i) and (ii) represent XRD patterns of 100h ball milled powder and corresponding sintered alloy of composition A. From a comparison point of view, some new intense peaks are observed in the XRD pattern of SPSed-A. Some of the peaks are indexed with the same phases as having in 100h ball-milled powders. Other than these phases, it was observed that some new phases Fe_5C_2 (mC28) and Cr_7C_3 (oP40) were evolved.

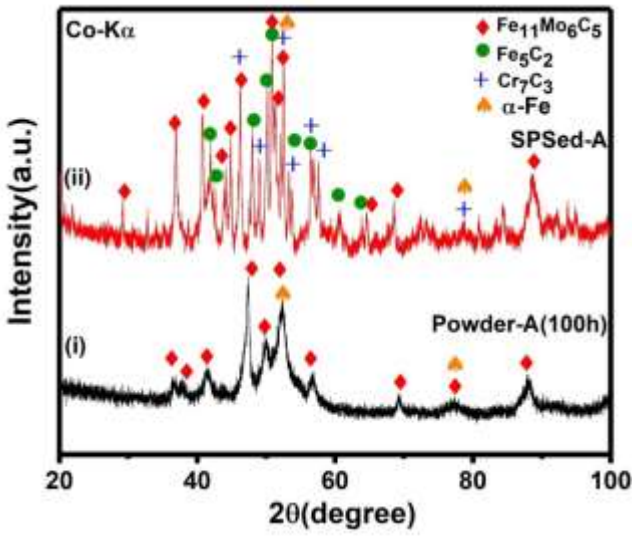

Fig. 6. 9: X-ray diffraction patterns of composition-A, (i) 100h ball-milled nanocomposite powder, and (ii) sintered composite at 800^{o}C.

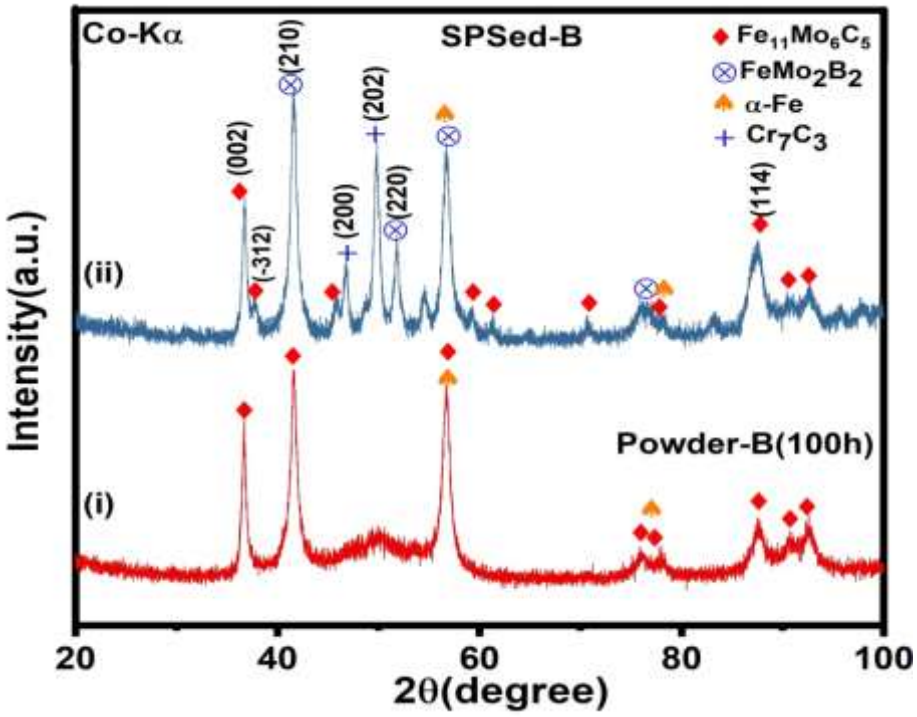

Fig. 6. 10: X-ray diffraction patterns of composition-B, (i) 100h ball-milled nanocomposite powder, and (ii) sintered composite sample.

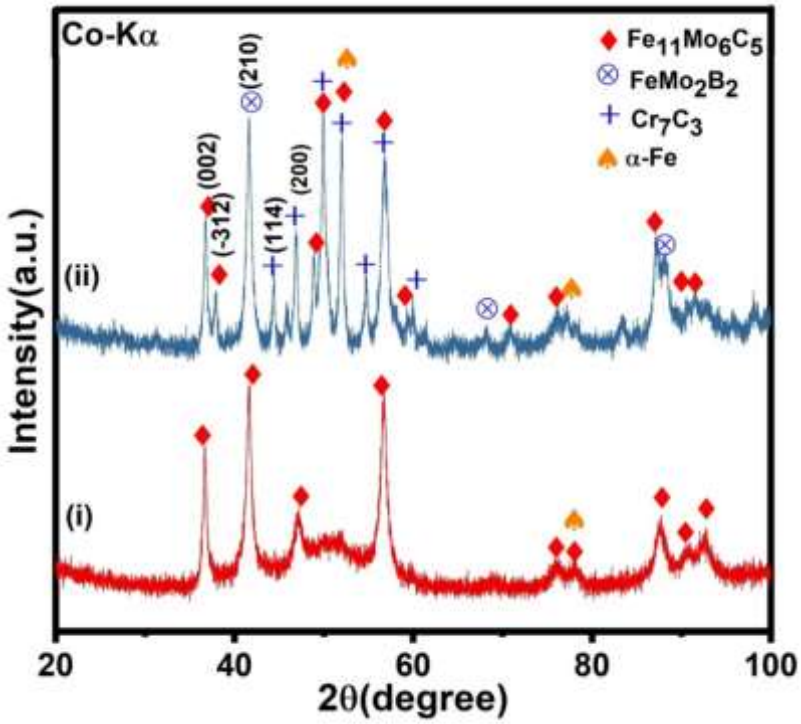

Fig. 6. 11: X-ray diffraction patterns of composition-C, (i) 100h ball-milled nanocomposite powder, and (ii) sintered sample

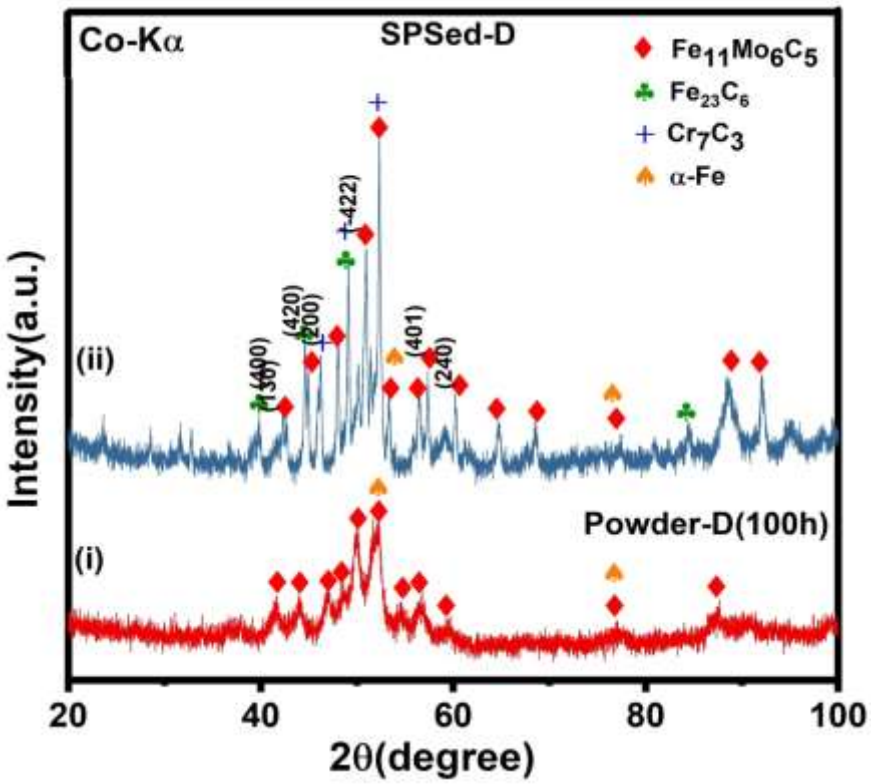

Fig. 6. 12: X-ray diffraction patterns of composition-D, (i) 100h ball-milled nanocomposite powder, and (ii) sintered composite sample.

X-ray diffraction patterns from starting powder (100h milled) and spark plasma sintered compacts of composition-B are presented in Fig. 6.10 (i) and (ii) respectively. The XRD pattern of 100h ball-milled powder evolves into two phases. However, in the case of the SPSed compact, the phase transformation and evolution of some new phases have taken place. Other than $Fe_{11}Mo_6C_5$ and α-Fe phases evolved in SPSed are Cr_7C_3 (oP40) and $FeMo_2B_2$ (tP10).

The XRD patterns of the sintered compact of SPSed-C and SPSed-D are shown in Fig. 6.11 and Fig. 6.12 respectively. The XRD pattern of SPSed-C evolves similar phases as evolved in SPSed-B. In the case of SPSed-D, the phase transformation takes place during the sintering of the powder. A new phase $Fe_{23}C_6$ (cF116) was evolved in SPSed-D. I have mentioned the reflections of some of the major phases in their diffraction patterns. All the information regarding phases that have evolved in sintered compacts as well as in 100h ball milled powders is given in Table 6.3.

Table 6. 3: Detail information of the phases evolved in the sintered samples

Sl.no.	Phase obtained	Pearson symbol	Space group (no.)	Samples	JCPDS no.
1	$Fe_{11}\ Mo_6C_5$	mC44	C2/m (12)	All	01-089-2311
2	Cr_7C_3	oP40	Pnma (62)	All	01-089-7244
3	Fe_5C_2	mC28	C2/c (15)	SPSed-A	00-051-0997
4	α-Fe	cI2	Im-3m (229)	All	00-006-0696
5	$Fe_{23}C_6$	cF116	Fm-3m (225)	SPSed-D	01-079-6180
6	$FeMo_2B_2$	tP10	P4/mbm (127)	SPSed-B, SPSed-C	01-089-3630

6.3.5 Morphology of Ball milled Powder

The SEM micrograph as shown in Fig. 6.13 A-B illustrates the size, shape, and morphology of the ball-milled powders of BMP-A, and BMP-B with milling time respectively. The histograms of the particle size distribution for different milling hours are shown in Fig. 6.13 (d-f) and also their values are given in Table 6.4. It was observed that the shapes of powder particles of all BMPs (ball-milled powders) are irregular throughout the milling. The morphology of particles of BMP-B changed into a plate-like shape during 10h to 70h of milling. The plate-like shaped fragments were broken to form smaller particles with spherical morphology, at the end of milling (~ 100h) owing to cumulative plastic deformation by the repetitive collision of the milling balls. In the case of a 100h powder sample of BMP-C and BMP-D, the faceted morphology has been observed. Figures 6.14C (c) and D(c) represent faceted morphology characteristics. In the XRD patterns of 100h ball-milled powders of sample BMP-C and BMP-D, a phase transformation has been seen (cf. fig.6.6 and 6.7), this may be one of the reasons for which faceted morphology has been developed. The shapes of particles are uniform and close to spherical in BMP-D as shown in Fig. 6.14D(c).

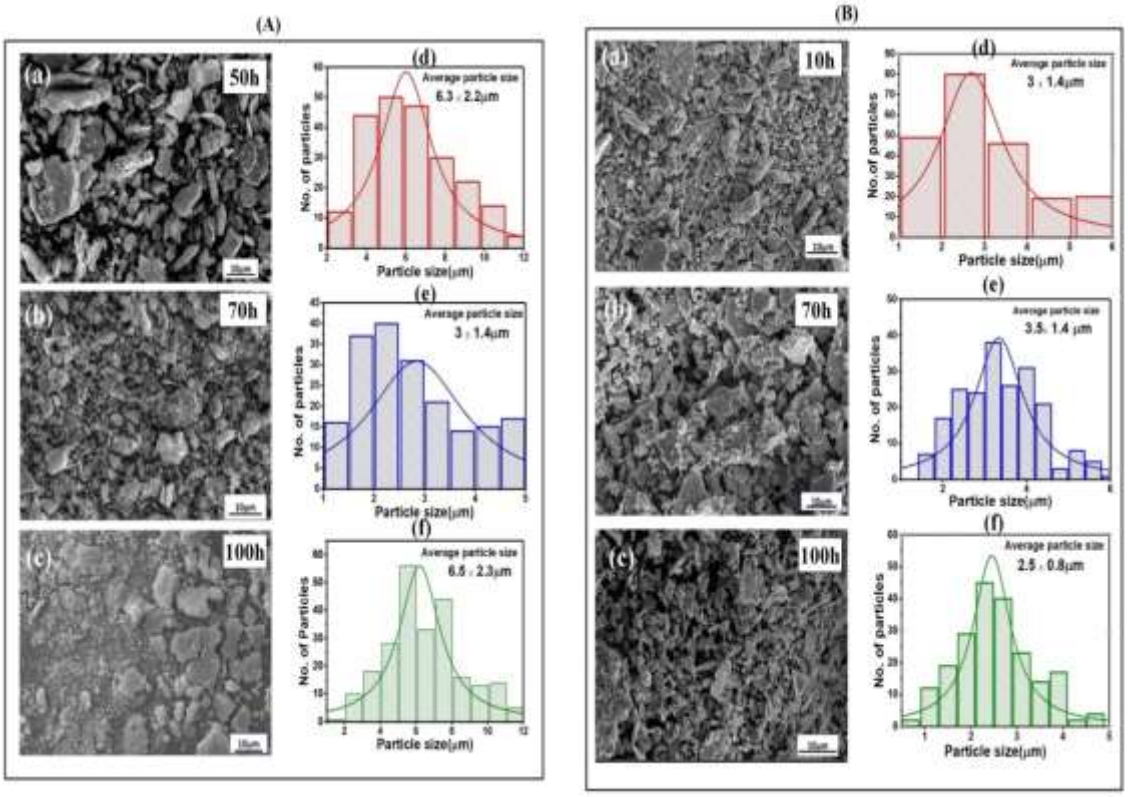

Fig. 6. 13: (a-c) shows an SEM micrograph of powders of (A) BMP-A, and (B) BMP-B with different milling times, and the histogram shown in (d-f) depicts their particle size distribution.

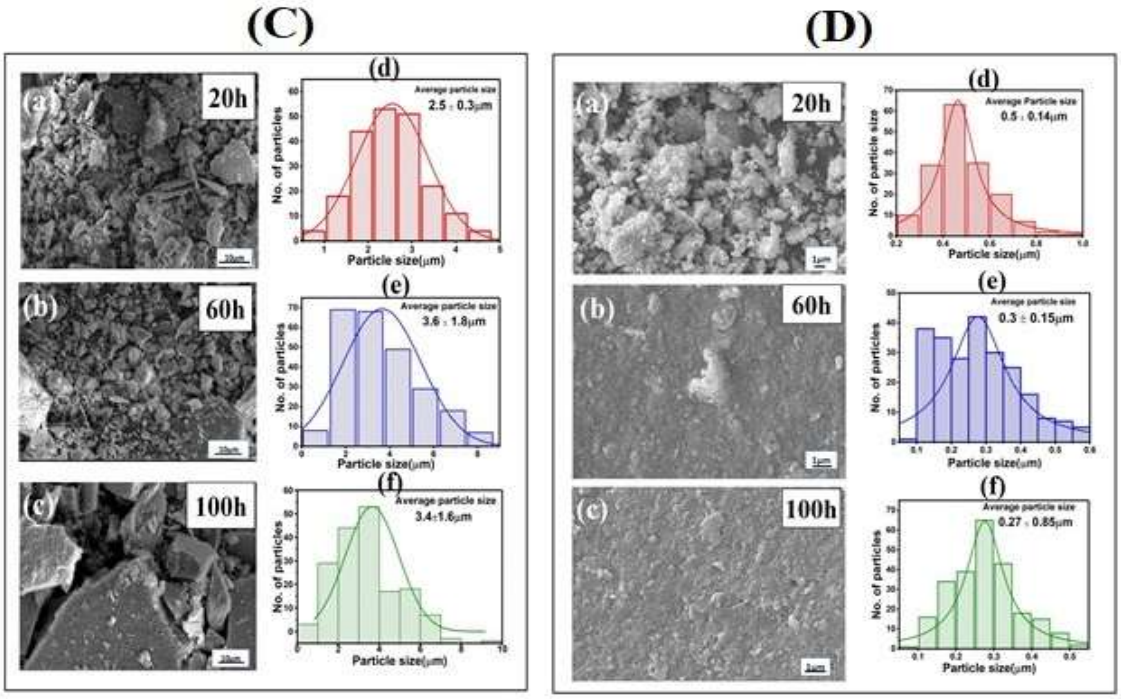

Fig. 6. 14: (a-c) shows SEM micrograph of powders of (C) BMP-C, and (D) BMP-D with different milling times and the histogram shown in (d-f) depicts their particle size distribution.

Table 6. 4: Variation of particle size (in μm) with milling time in ball-milled Powder samples

	BMP-A			BMP-B		
	50h	**70h**	**100h**	**10h**	**70h**	**100h**
Avg. Particle size (μm)	6.3±2.2	3±1.5	6.5±2.3	3.0±1.4	3.5±1.4	2.5±0.8
	BMP-C			**BMP-D**		
	20h	**60h**	**100h**	**20h**	**60h**	**100h**
Avg. Particle size (μm)	2.5±0.3	3.6±1.8	3.4±1.6	0.5±0.1	0.3±0.1	0.3±0.8

6.3.6 Morphology of Sintered Alloy

Figure 6.15(a) represents the area selected for the elemental mapping of SPSed-A, while Fig. 6.15 (b) shows the overall elemental distribution within the selected area of the microstructure. The SEM-EDS chemical composition of individual elements within the selected area is shown in Fig. 6.15 (c). It is evident from fig. 6.15(c) that the grey color region in the SPSed-A is rich in Fe, O, and Mo and lean in Cr, Si, and C.

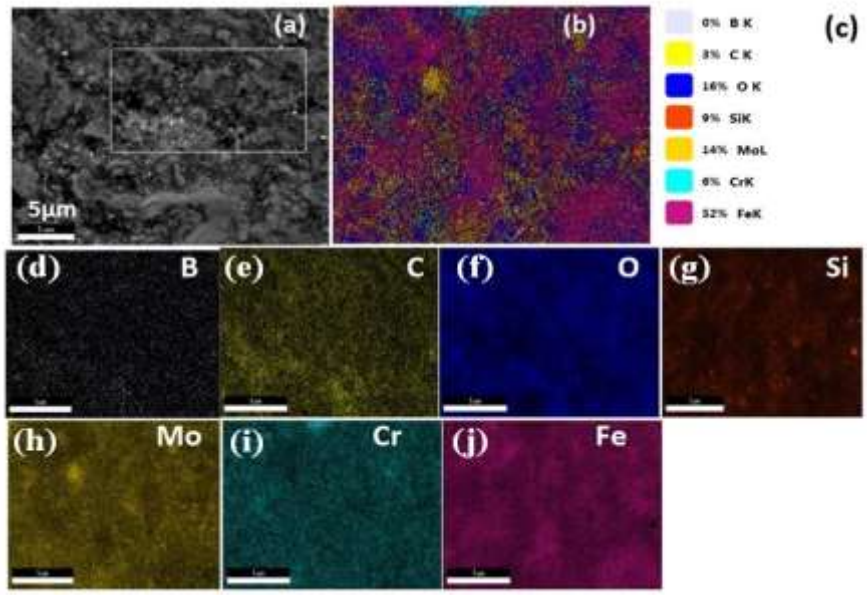

Fig. 6. 15: SEM micrograph of SPSed-A (a) spark plasma sintered at 800 ^{o}C and showing selected area for elemental mapping; (b) distribution of all the elements within the selected area; (c) SEM-EDS chemical composition of individual elements corresponding to the selected area; (d-j) individual elemental distribution within the selected area.

Table 6. 5: Elemental composition of SPSed-A sample by point EDS analysis.

Element	Full area	Spot-1	Spot-2
	at%	at%	at%
B	0	0	0
C	9.1	17.6	14.5
O	34	-	-
Si	3.1	3.6	1.7
Mo	5.1	23.5	16
Cr	3.5	1.7	3
Fe	44.2	53.6	63.5
W	1	-	1.3

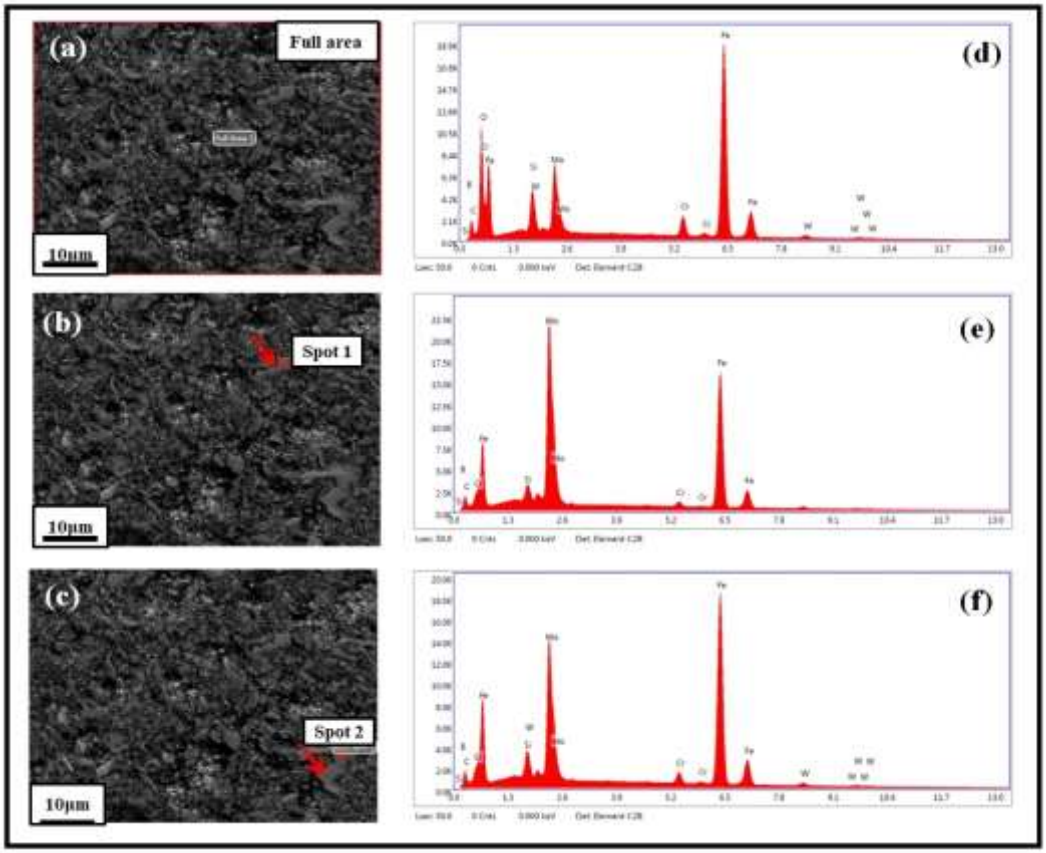

Fig. 6. 16: (a-c) SEM images of SPSed-A sample at the same magnification, showing full area, spot 1, and spot 2; (d-f) EDS spectrum of the marked area.

The SEM micrograph of the SPSed-A sample at 800 ^{o}C and 50MPa with the same magnification is illustrated in Fig. 6.16 (a-c). The SEM-EDS spectrum at the full area, small grey region (spot-1), and large grey region (spot-2) are shown in Fig. 6.16 (d-f). The distributions of all the elements in the SPSed sample are non-uniform and their compositions are shown in Table 6.5. Full area EDS-spectrum shows that Fe and O are rich in this area, while the marked spots are rich in Fe and Mo. The presence of the major amount of oxygen after that Fe, it is evident that this sample has a huge amount of impurity, which is why SPSed-A is very poorly densified (~5.2g/cc) and is not well sintered.

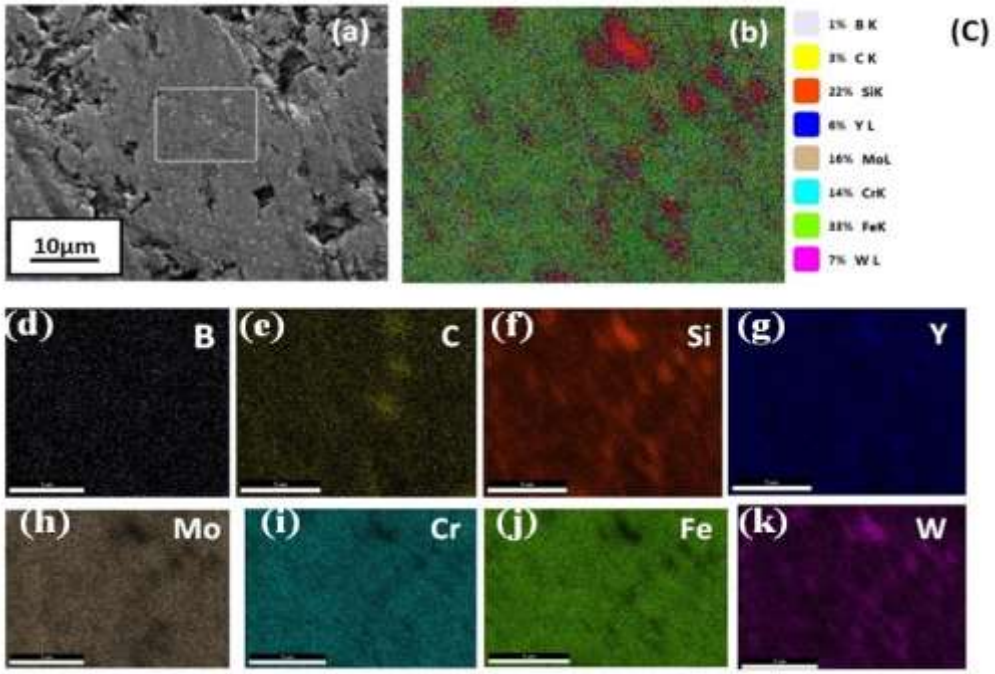

Fig. 6. 17: SEM micrograph of SPSed-B (a) spark plasma sintered at 800 ^{o}C and showing selected area for elemental mapping; (b) distribution of all the elements within the selected area; (c) SEM-EDS chemical composition of individual elements corresponding to the selected area; (d-k) individual elemental distribution within the selected area.

The chemical composition of the individual elements corresponding to the selected area in the SPSed-B sample as shown in Fig. 6.17(a) is given in Fig. 6.17(c). The distribution of elements is non-uniform as shown in Fig. 6.17 (b). It is evident from fig. 6.17(c) that Fe, Si, Cr, and Mo are rich in this region. The SEM microstructure of SPSed-B (cf. fig. 6.18(a)) shows that small white spots are uniformly distributed throughout the sintered sample. For knowing their composition EDS analysis was done. The SEM microstructure of full area, spot-1, and spot-2 are shown in Fig. 6.18(a-c). Figure 6.18 (d-f) shows the EDS spectrum corresponding to the aforesaid region. The

chemical composition of the individual elements corresponding to the full area, spot-1 and spot-2 are given in Table 6.6. It was observed that spot-1 and spot-2 are rich in C and also W was found in lean amounts. The extra tungsten and C elements may come from tungsten vials and tungsten carbide balls.

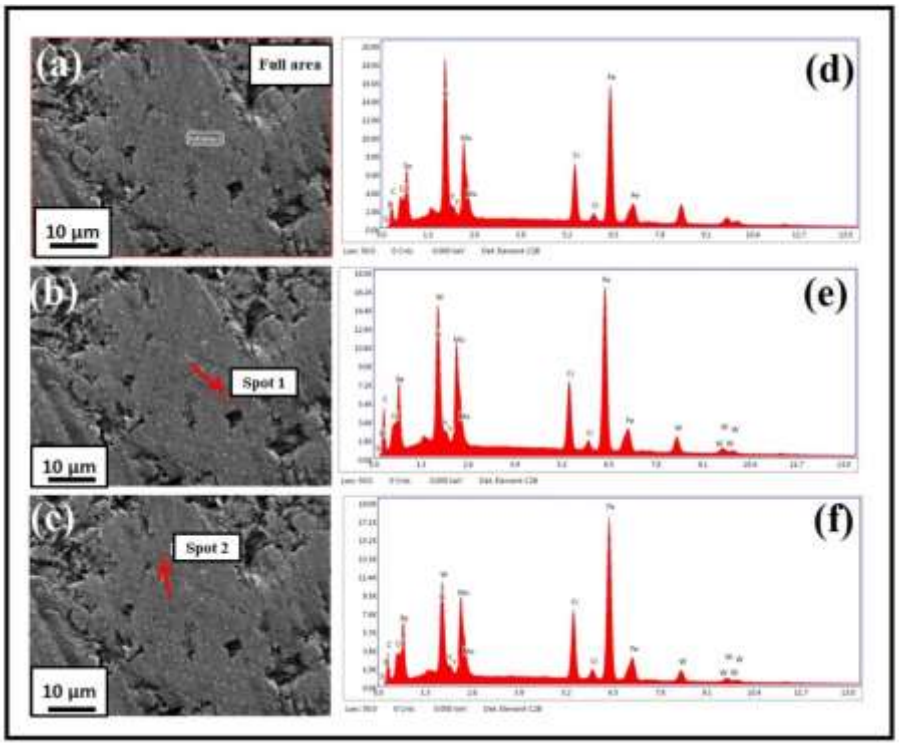

Fig. 6. 18: (a-c) SEM images of SPSed-B sample at the same magnification, showing full area, spot 1, and spot 2; (d-f) EDS spectrum of the marked area.

Table 6. 6: Elemental composition of SPSed-B sample by point EDS analysis

Element	Full area	Spot-1	Spot-2
	at%	at%	at%
B	0	0	0
C	28.3	43.2	31.8
Si	20.1	2.9	3.1
Y	2.8	0.9	0.8
Mo	6.6	7.6	7.5
Cr	10.4	10.1	13.1

Fe	31.8	31.0	39.9
W	-	4.3	3.9

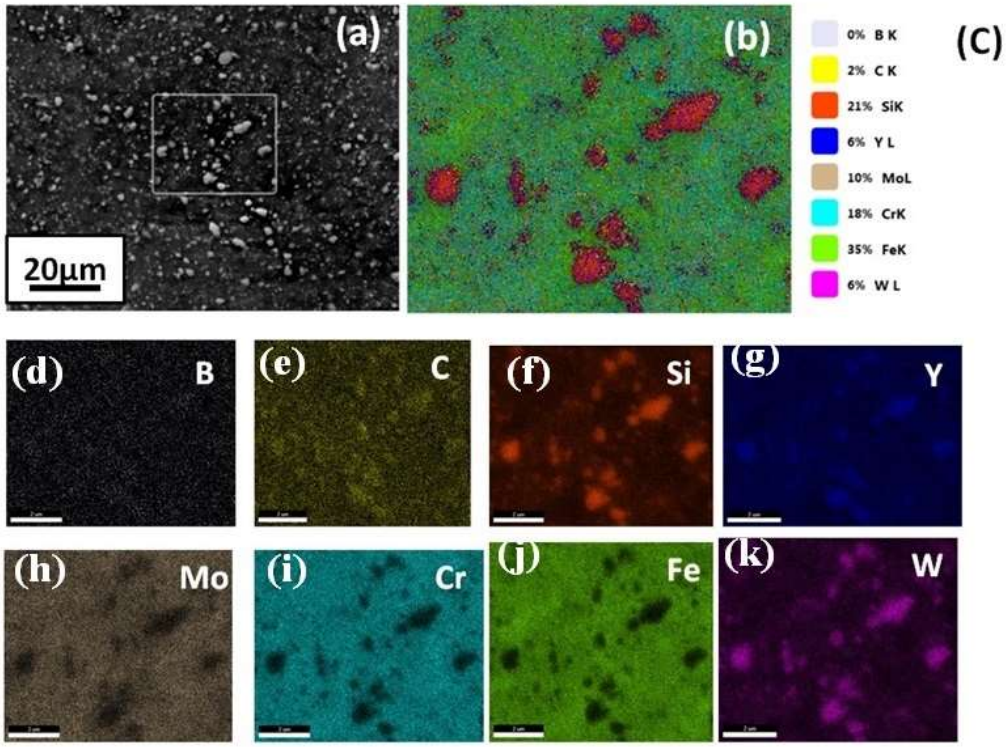

Fig. 6. 19: SEM micrograph of SPSed-C (a) spark plasma sintered at 800 ^{o}C and showing selected area for elemental mapping; (b) distribution of all the elements within the selected area; (c) SEM-EDS chemical composition of individual elements corresponding to the selected area; (d-k) individual elemental distribution within the selected area.

Figure 6.19(b) shows the elemental distribution of the SPSed-C sample of the selected area as shown in Fig. 6.19(a). The SEM-EDS chemical compositions of individual elements corresponding to the selected area are shown in Fig. 6.19 (c). The EDS analysis of the aforesaid area shows that Fe and Si are rich in this area, while C and Y are lean. The SEM micrograph as shown in Fig. 6.20 (a), shows a non-uniform distribution of white particles-like features embedded in the matrix. I have considered two white features and their names spot-1(smaller particle) and spot-2 (bigger particle). The EDS spectrum of the full area, spot-1, and spot-2 are shown in fig. 6.20 (a-c) are shown in fig. 6.20(d-f). The chemical composition of the individual elements corresponding to full area, spot-1, and spot-2 are given in Table 6.7. It was observed that the full area and spot-1 are rich in Fe, Cr, and C elements, although spot-2 is rich in W and C. Therefore, it was confirmed that the spot-2 is a contaminant from tungsten vials or balls.

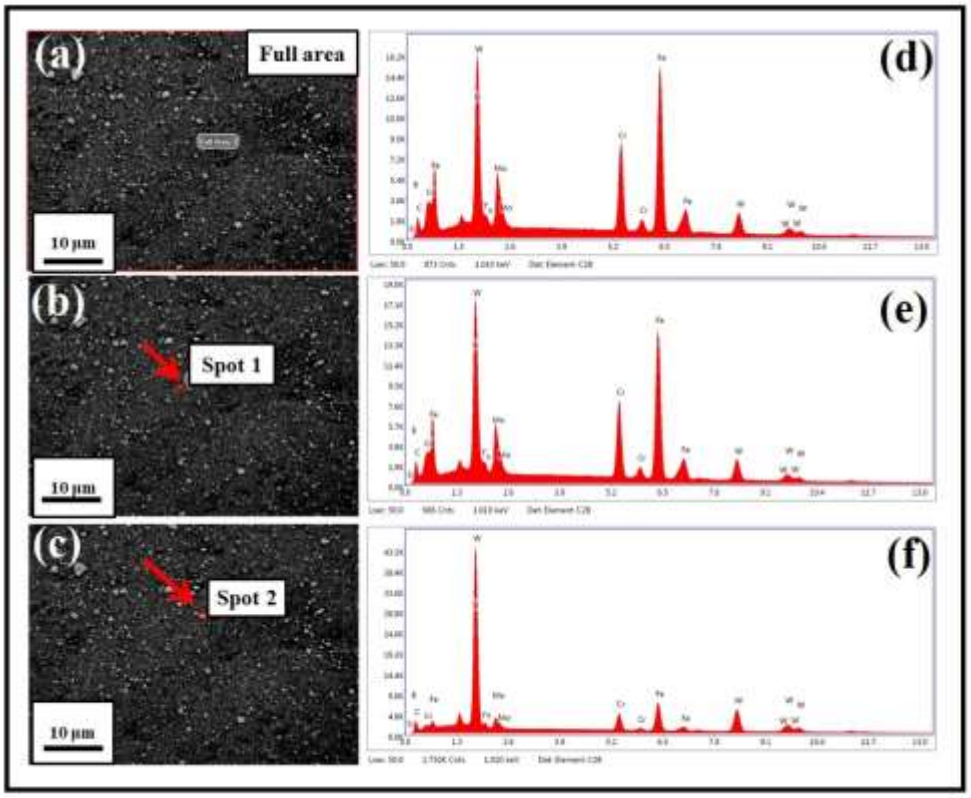

Fig. 6. 20: (a-c) SEM images of SPSed-C sample at the same magnification, showing full area, spot 1, and spot 2; (d-f) EDS spectrum of the marked area.

Table 6. 7: Elemental composition of SPSed-C sample by point EDS analysis

Element	Full area	Spot-1	Spot-2
	at%	at%	at%
B	0	0	0
C	13.9	20.4	41.3
Si	4	3.6	3
Y	1	1.1	1.2
Mo	5.6	5.5	3.2
Cr	19.5	17.4	9.3
Fe	47.2	43.3	18.8
W	8.8	8.8	23.1

The SEM micrograph of a sintered compact sample of SPSed-D has been shown in Fig 6.21(a). The micrograph depicts three contrasts, grey, black, and white. Figure 6.21 (b) shows the overall elemental mapping of the selected area (cf. fig. 6.21(a)). The chemical compositions of individual elements in this area are shown in Fig. 6.21 (c). Figure 6.21(d-l) shows individual elemental distribution within the selected area. All the elements are non-uniformly distributed in the selected area. The SEM-EDS analysis shows that Fe, Cr, and Mo are rich in this region. Oxygen is also present in considerable (~10%) quantity. Figure 6.22 (a-c) represents the SEM micrographs of the full area, white contrast (spot-1), and grey contrast (spot-2) were marked. The EDS spectrums of these aforesaid regions are shown in Fig. 6.22 (d-f). The elemental compositions of these aforesaid regions are summarized in Table 6.8. Table 6.8 illustrates that a great amount of O elements is present in the full area and spot 2 next to Fe. The presence of the O element may be one of the reasons for its moderately poor densification. The density of the sintered sample of SPSed-D (~6.2g/cc) is lower than the as-cast density (~7.5g/cc). Oxygen element plays a crucial role in densification during the sintering process.

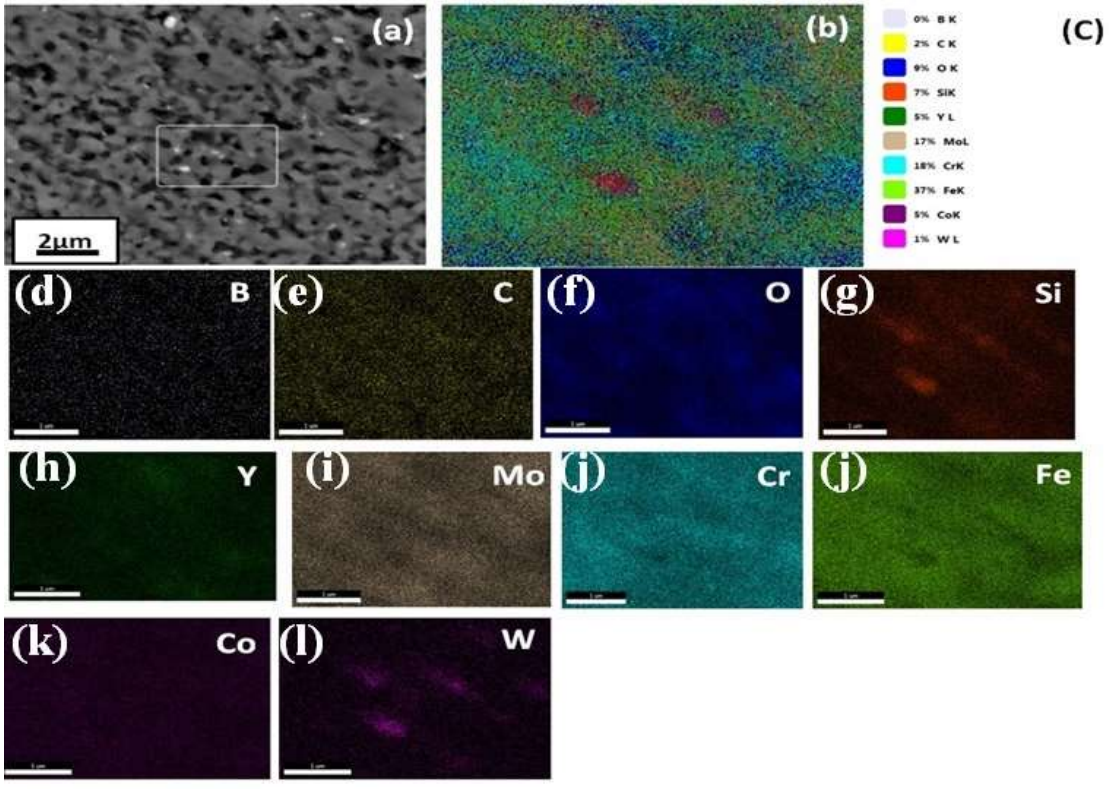

Fig. 6. 21: SEM micrograph of SPSed-D (a) spark plasma sintered at 800 ^{o}C and showing selected area for elemental mapping; (b) distribution of all the elements within the selected area; (c) SEM-EDS chemical composition of individual elements corresponding to the selected area; (d-l) individual elemental distribution within the selected area.

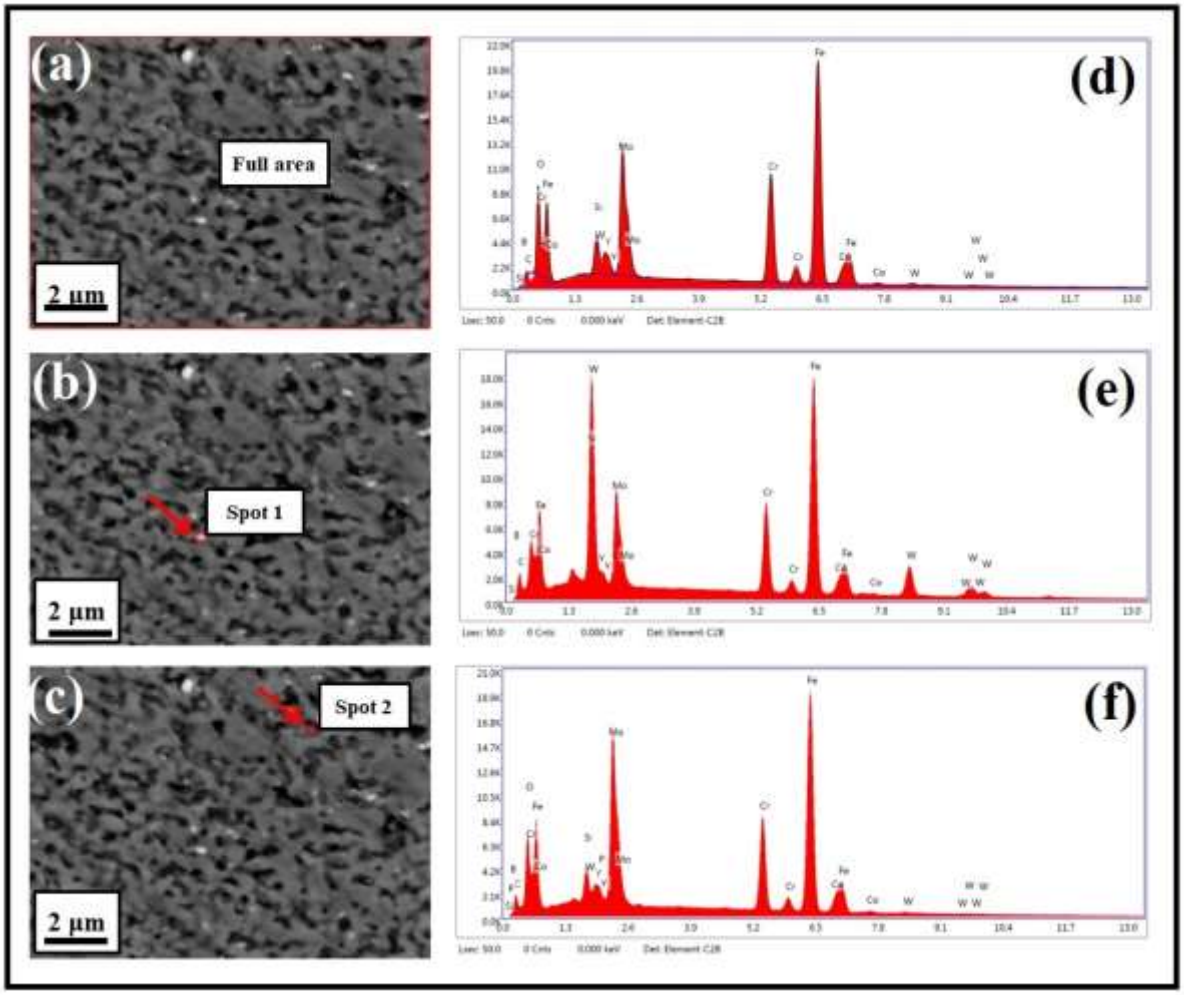

Fig. 6. 22: (a-c) SEM images of SPSed-D sample at same magnification, showing full area, spot 1, and spot 2; (d-f) EDS spectrum of the marked area.

Table 6. 8: Elemental composition of SPSed-C sample by point EDS analysis

Element	Full area	Spot-1	Spot-2
	at%	at%	at%
B	0	0	0
C	3.9	18.6	7.3
O	27.9	-	26.7
Si	2.9	2.1	2.4
Y	1.3	1.1	0.9
Mo	7.9	8.5	10.5

Cr	14	14.3	12
Fe	38.9	44	37.4
Co	2.7	2.7	2.5
W	0.5	8.7	0.3

6.3.7 Nature of Indentation of sintered alloys at different loads

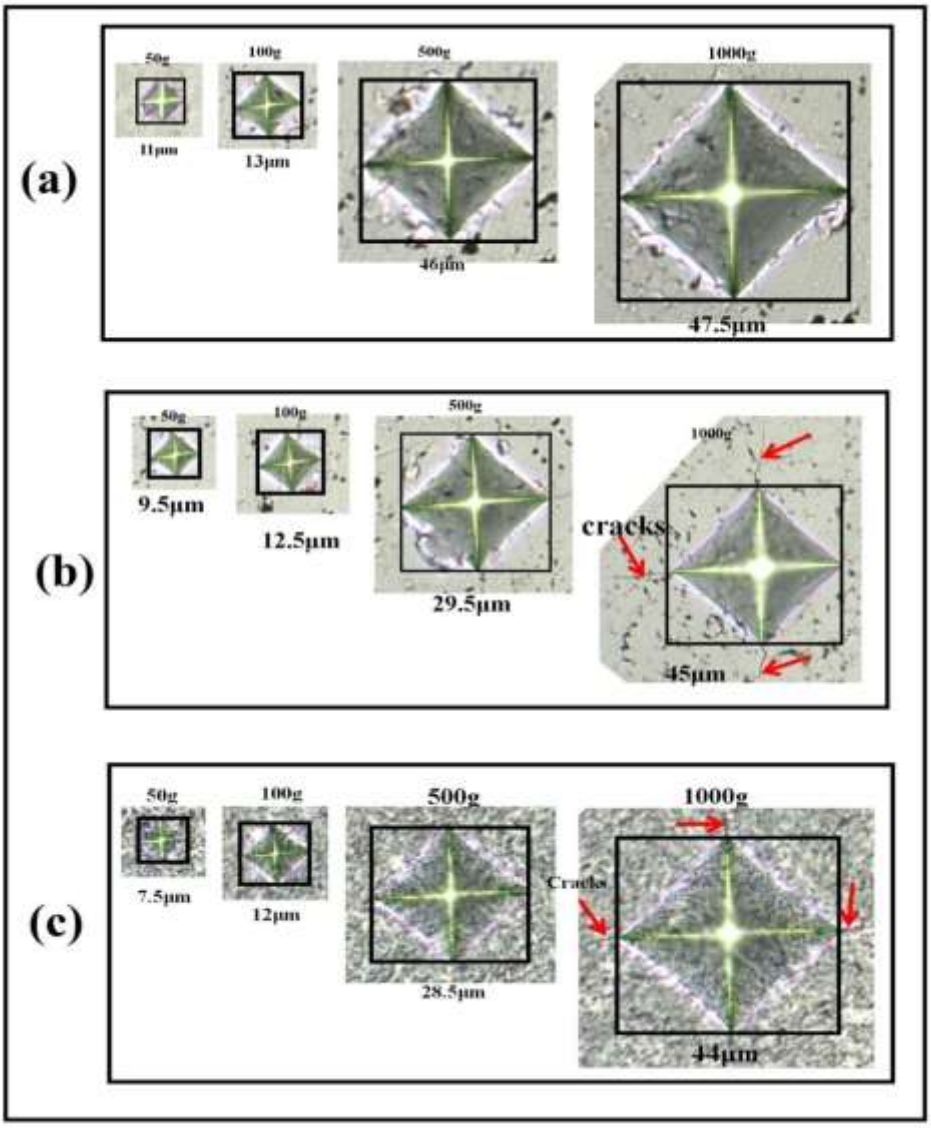

Fig. 6. 23: Optical images of indentation impression from various regions for sintered alloys (a) SPSed-B, (b) SPSed-C, and (c) SPSed-D, showing the nature of indentation with load up to fracture.

Fig.6.23 (a-c) displays the optical micrograph of the indentation impression of sintered alloys from various regions at different loads. The figure does not include SPSed-A as the sample was having

a lot of defects that were also reflected in the lowest density (~5.02 g/cc) as well as in the value of H_v (~3GPa). It is to be noted that the initiation of cracks is observed at their corner in SPSed-C and SPSed-D at the maximum applied load of 1000g as shown in Fig. 6.23 (b and c) by an arrow marked. The absence of a crack at the corner of the SPSed-B sample suggests that this has better toughness as compared to SPSed-C and SPSed-D. It was observed that the size of the indentation impression in all sintered samples as shown in Fig. 6.24 (a-d), increases at a slower rate at low load but it drastically increases at high load conditions.

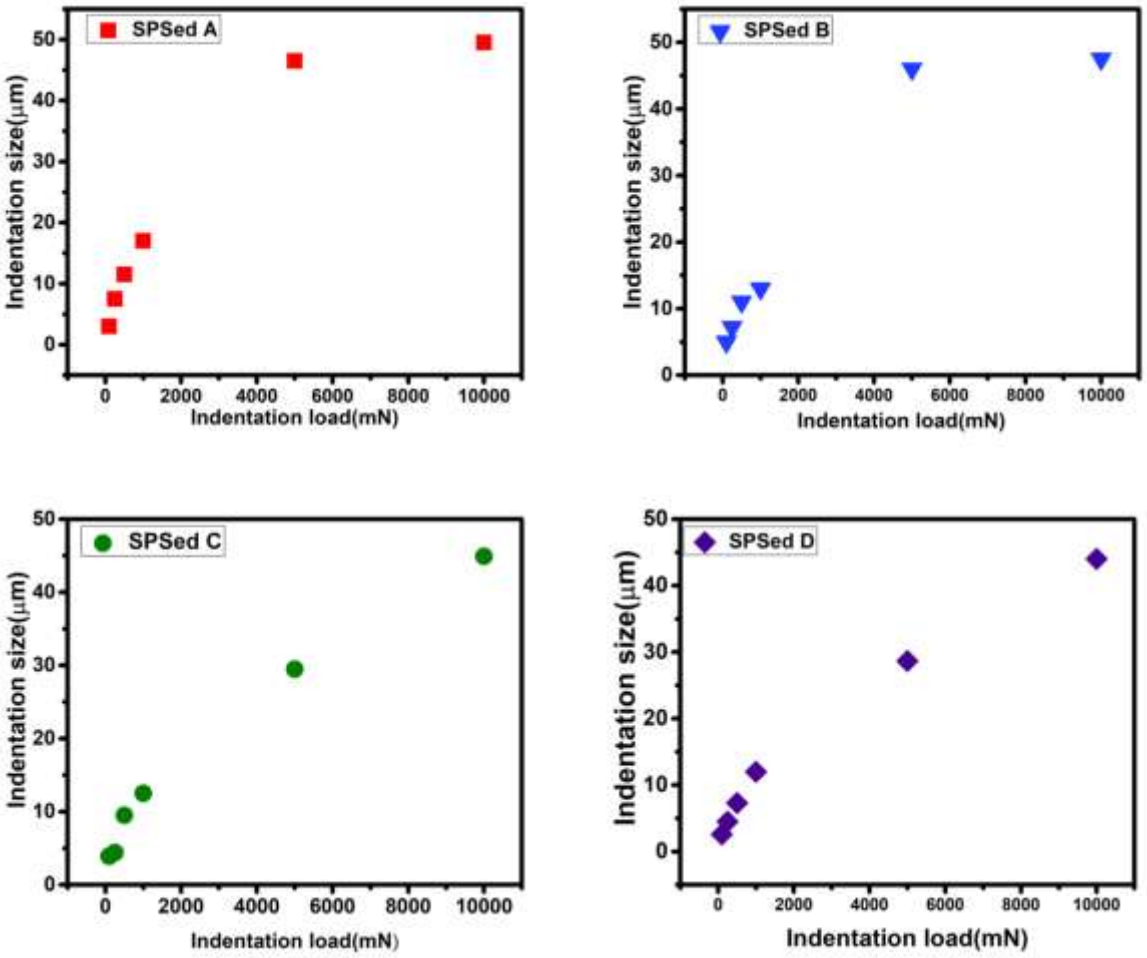

Fig. 6. 24: Shows the nature of variation of indentation size with load in (a) SPSed-A, (b) SPSed-B, (c) SPSed-C, and (d) SPSed-D.

The microhardness and elastic modulus of sintered samples were determined from a micro indentation experiment. Fig. 6.25 (a-d) shows the hardness versus load characteristic of the SPSed alloys. It was observed that in SPSed-A, the Vickers hardness value continuously decreases with

loads shown in Fig. 6.25(a), it shows an indentation size effect (ISE)[230] while in other SPSed samples, the microhardness value first increases with the applied load and then become constant or decreases as shown in Fig. 6.25 (b-d), reverse ISE has been observed[230], [231]. The microhardness values of these samples at various loads are given in Table 6.9. Also

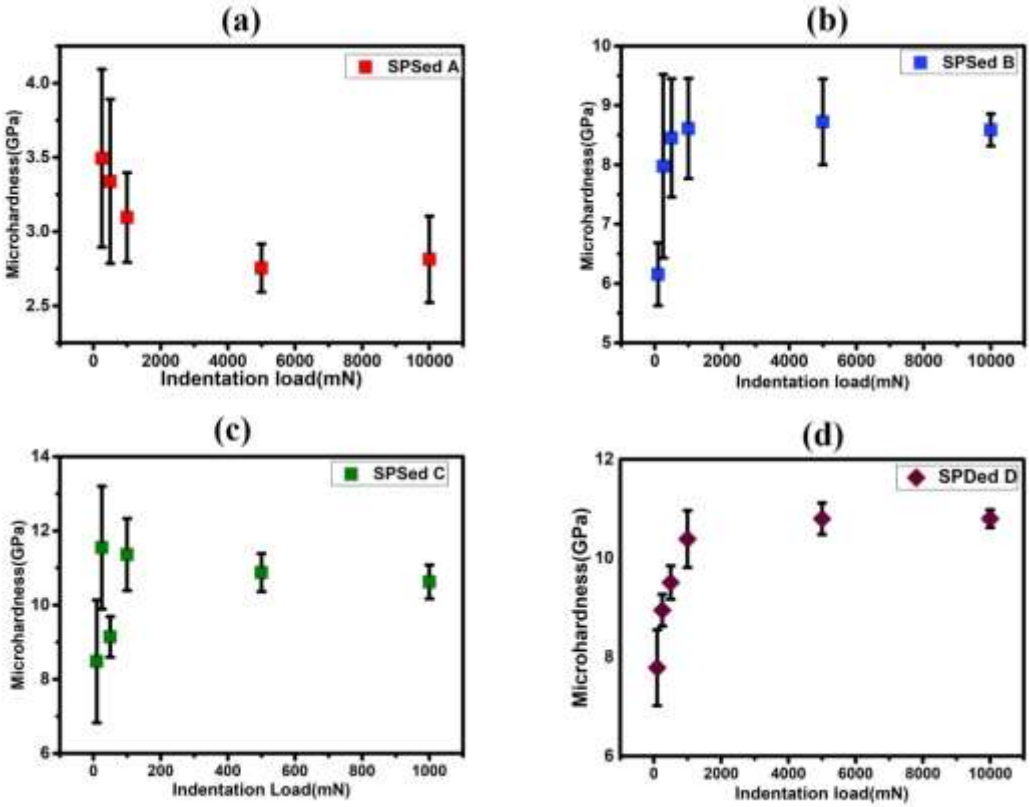

Fig. 6. 25: Variation of hardness (GPa) for load (mN) for the SPSed alloys (a) SPSed-A, (b) SPSed-B, (c) SPSed-C, and (d) SPSed-D.

I have measured the diagonal length of indentation impressions by of indentation impressions by using Image J software. The Vickers hardness value in GPa was calculated from the modified standard formula[167],

$$\mathbf{H = 1.654*9.81P/d^2}$$

Where P is the load (g) and d is the indentation diagonal length in μm. A comparative study has been done for the comparison of hardness at an indentation load of 100g among the entire sintered alloys as shown in Fig. 6.28 (a). The maximum Vickers hardness value was found in the SPSed-C composite having a value of ~12 GPa, while the minimum microhardness was found in SPSed-A (i.e. ~ 3GPa) at 100g indentation load.

Table 6. 9: Indentation diagonal length, microhardness data in GPa at various loads are displayed

	Indentation diagonal length, (μm)				**Vickers hardness (H_V) with std. dev. (in GPa)**				
Load(g)	**d_A**	**d_B**	**d_C**	**d_D**	**SPSed-A**	**SPSed-B**	**SPSed-C**	**SPSed-D**	**Remarks**
10	3	5	3.9	2.6	3±0.8	6±0.5	8.5±1.6	7.7±0.7	No cracks
25	7.5	7.2	4.4	4.5	3.5±0.7	8±1.5	11.5±1.6	9±0.3	No cracks
50	11.5	11	9.5	7.3	3.3±0.5	8.5±1	9±0.5	9.5±0.3	No cracks
100	17	13	12.5	12	3±0.3	8.6±0.8	11±0.9	10±0.6	No cracks
500	28.5	28	29.5	28	2.7±0.1	8.7±0.7	10.8±0.5	10.7±0.3	Palmqvist Crack in SPSed-C
1000	49.5	47.5	45	44	2.8±0.3	8.6±0.3	10.6±0.4	10.8±0.2	Palmqvist Crack in SPSed D

6.3.8 Determination of Indentation Fracture toughness (K_{IC})

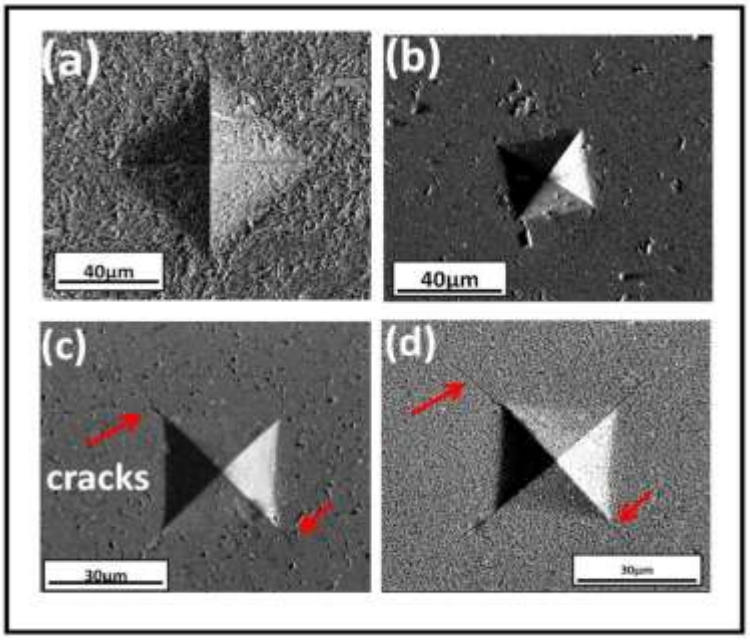

Fig. 6. 26: SEM micrographs showing indentation impression at 1000g load (a) SPSed-A, (b) SPSed-B, (c) SPSed-C, and (d) SPSed-D. The arrow marks show radial cracks.

Figure 6.26 shows SEM micrographs of the indentation impression of sintered samples at 1000g applied load. It was observed that in SPSed-C and SPSed-D, very fine radial cracks are formed from the indentation corner at 1000g indentation load as shown in Fig. 6.26 (c and d) while SPSed-A and SPSed-B are cracked-free are shown in Fig. 6.26(a and b). For evaluation of the fracture toughness of these samples the Palmqvist method [170][169] was used. The fracture toughness of any brittle material can be estimated by using the expression written below,

$$K_{IC} = 0.035\ \Phi^{(-3/5)} H_v\ (a/L^{1/2})(H/E)^{-2/5}$$

Where K_{IC} = Indentation fracture toughness, Φ = Constraint factor and has been taken 2.5[172], H_v = Vickers microhardness in GPa, E = Young's modulus in GPa, a= half of the indentation size (μm), and L = length of Palmqvist crack. The values of fracture toughness of sintered composites are given in Table 6.10.

Table 6. 10: Fracture toughness of sintered composites at 1000g indentation load.

Sample	Estimation method	Half of indentation size, a (μm)	Crack length, L (in μm)	Fracture toughness, K_{IC} (MPa.m$^{1/2}$)
SPSed-C	Palmqvist method	21.6	16	3.60
SPSed-D	Palmqvist method	21.3	18.7	3.22

6.3.9 Determination of Yield strength (σ_o), Meyer's exponent (n), material constant (K)

The 0.2% offset yield strength of the 100h ball milled sintered powder can be calculated from simple hardness measurements using the following expression[173];

$$\sigma_o = (VHN/3)0.1^{n-2}$$

Where σ_o = 0.2% offset yield strength and n is Meyer's exponent and related to the material capacity of work hardening. The variation of hardness with load can be analyzed using Meyer's law. The variation of load can be related to the diagonal length (d) as:

$$P = Kd^n$$

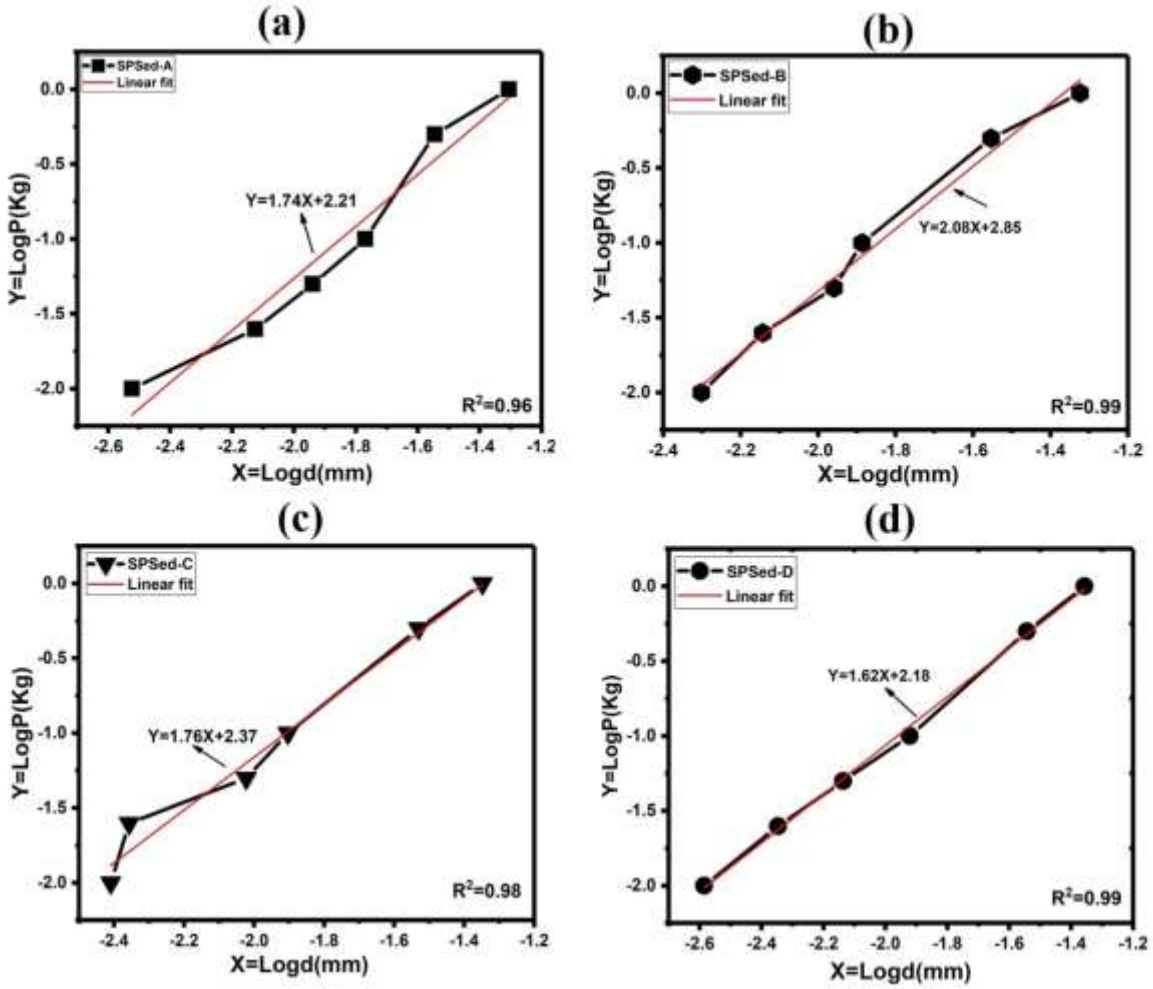

Fig. 6. 27: Log P vs Log d plots for sintered composite, (a) SPSed-A, (b) SPSed-B, (c) SPSed-C, and (d) SPSed-D. The lines are the linear fit to the data and R^2 is the correlation coefficient and has a value in the range 0.96-0.99.

Where P is the applied load (in Kg), d is the indentation diagonal length (in mm), K is the material constant related to the resistance of the metal to penetration, and n is Meyer's exponent. In the ideal case, Meyer's exponent has a value of 2. However, the value of n varies from material to material. It is worthwhile exercise to determine these parameters for present material and understand their behavior. From the present experimental data, the LogP vs Logd curves for sintered alloys have been plotted as shown in Fig. 6.27(a-d). The values of Meyer's exponent (n) and LogK are given in Table 4.11. It was observed that the value of 'n' lies in the range of (~1.6-2) and it is less than 2. Meyer's exponent values for all sintered composites are found to be different. This change is due to microstructural and structural variations in them, as different alloying additions have been taken. It was observed that σ_o is found maximum for SPSed-D (~8

GPa). The Meyer's exponents for SPSed-B is higher (n~2) and also the ratio of VHN/σ_o is also highest (=3.62).

Table 6. 11: Values of average VHN, E, n, Log K, and σ_o of Sintered alloy at 100g load

As-cast alloys	VHN (GPa) (100g load)	Reduced Elastic modulus (E)(GPa)	n	LogK	σ_o (GPa) (100g load)	VHN/σ_o
A	3	66	1.74	2.08	1.82	1.64
B	8.5	188	2.08	2.91	2.35	3.62
C	11	206	1.76	2.35	6.36	1.72
D	10	180	1.62	2.11	7.98	1.25

6.3.10 Determination of Plastic criterion (R_w) and Percentage of Elastic recovery (%R)

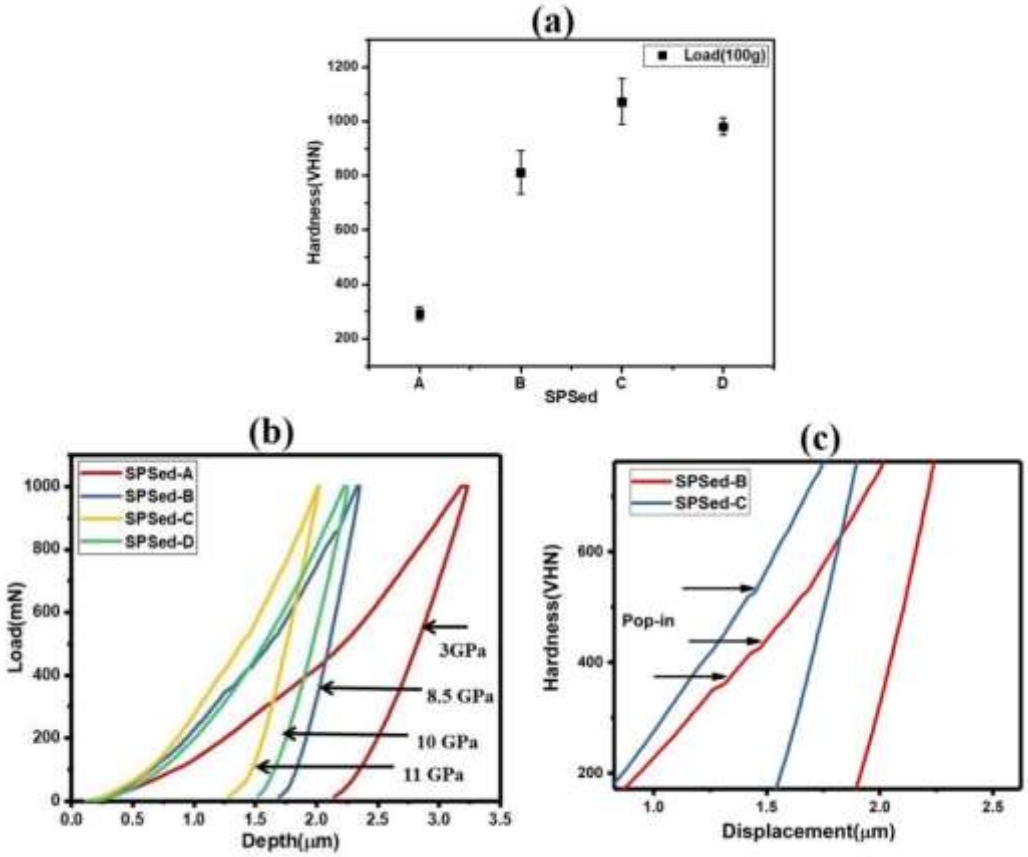

Fig. 6. 28: (a) Comparison of hardness (VHN) at indentation load of 100g among all sintered composites; (b) Load-displacement (p-h) plot response of sintered composite at 100g load; (c) showing pop-in marks in unloading (P-h) curve.

The load-displacement (P-h) curves for SPS samples are shown in Fig. 6.28 (b). The maximum depth of penetration for SPSed-A, B, C, and D are found to be 3.22, 2.35, 2.02, and 2.24μm respectively. The maximum depth of penetration was observed in SPSed-A; hence it shows very poor hardness. Higher the slopes of unloading curve in the P-h plot represent higher stiffness of the material. In the present investigation, the P-h plot of the SPSed-C sample has higher stiffness. A small pop-in (displacement discontinuity) event has been observed in the loading part of the P-h curve of SPSed-B and SPSed-C alloys (fig. 6.28(c)) while SPSed-A and SPSed-D have smooth curves. The net amount of work done during the indentation test can be calculated by the considering area enclosed by the P-h curve. Three important parameters were estimated from P-h curves. These are as follows:

(i) A plastic criterion R_w [178], [179] is defined as the ratio of plastic work (W_p) to the total work ($W_T = W_P + W_e$) and this ratio is expressed as a percentage and is given by the expression,

$$\% \, R_W = \frac{WP}{WT} x \, 100$$

(ii) The elastic recovery, R[120] can be defined as the ratio of the final depth of the indentation (h_f) to the maximum penetration depth (h_{max}) of the indenter,

$$\textbf{Elastic recovery, } R = h_f/h_{max}$$

(iii) Percentage of elastic recovery rate (%R) [120] of displacement on the unloading curve can be expressed as;

$$\%R = \frac{(hmax - hf)}{hmax} X100\%$$

Table 6. 12: The Mechanical properties of the tested sintered alloy estimated from the P-h plot at 100g indentation load

SPSed sample	W_P (10^{15} J)	W_e (10^{15} J)	W_T (10^{15} J)	R_W (in %)	h_f (μm)	h_{max} (μm)	R (h_f/h_{max})	%R
A	476	972	1448	32	2.14	3.22	0.66	33.5
B	1663	3718	5382	30	1.69	2.35	0.72	28
C	226	440	667	34	1.28	2.02	0.63	36.6
D	451	687	1139	39.5	1.52	2.24	0.68	32

The parameter R_w is calculated for sintered samples and found to be in the range of ~ (30-40%). This result indicates that elastic deformation due to indentation is more as compared to plastic deformation in the materials. It has been observed that SPSed-D has a maximum value of R_W (~40%), which shows SPSed-D has a good amount of plasticity among all sintered compacts. Generally, the limit of elastic recovery lies in the range of $0 \leq h_f/h_{max} \leq 1$. The present sintered alloys have elastic recovery values in the range of 0.63 to 0.72. The values of all these parameters as described above have been given in Table 6.12.

The degree of elastic recovery i.e., the ratio of hardness to elastic modulus (H/E), the ratio of hardness to density (H/ρ), and the specific stiffness (E/ρ) of the present material is also calculated and their values are given in Table-6.13. The H/E, H/ρ, and E/ρ ratios are found to be in the range of (0.045-0.055), (0.6-1.6), and (13-29) respectively.

Table 6. 13: Some important Mechanical properties of SPSed alloy at 100g load.

SPSed sample	H (GPa)	E (GPa)	H/E	H/ρ	E/ρ
A	3	66	0.045	0.59	13.14
B	8.5	188	0.045	1.11	24.54
C	11	206	0.053	1.44	27.03
D	10	180	0.055	1.59	28.66

6.4 Discussion

6.4.1 Microstructure, Phase/Structure Analysis

The optical as well as SEM microstructures of sintered samples show that all the samples have uniform microstructure and get well sintered except SPSed-A. The morphology of ball milled powder of sample BMP-A and BMP-B changes with milling time. At the end of milling (~100h) spherical morphology was achieved in these samples. In the case of 100h ball milled powder of BMP-C and BMP-D, the faceted morphology (cf. fig.6.14 (c) & (D)) has been observed. A similar kind of morphology was also observed in the work of Singh et al.[184].

The XRD results of alloys prepared through Cu-mould casting gave multiple crystalline phases, $Fe_{11}Mo_6C_5$ (mC44), α-Fe (cI2), Fe_5C_2 (mC28), Fe_3C (oP116), Fe_3W_3C (cF112), and Cr_7C_3 (oP40)

as already discussed in chapter-4. These alloys when processed through high energy ball milling only two phases retain at the end of 100h of milling. They are α-Fe (ferrite) and $Fe_{11}Mo_6C_5$. It was noticed that in the XRD patterns of BMP-C and BMP-D a phase transformation taking place, this is one of the reasons that faceted morphology was observed in BMP-C and BMP-D. Further, 100h ball-milled powders consolidated through the SPS technique survived after 100h of milling indicating an excellent propensity of retention of these phases. However, SPSed samples give rise to additional crystalline phases $Fe_{23}C_6$ (cF116) and $FeMo_2B_2$ (tP10). These phases are also observed by many researchers[182][117] during the devitrification process. This means phase transformation takes place during the process of SPS in addition to consolidation. The phases evolved in these alloy systems after processing through ball milling and SPS are summarized in Table 6. The SEM-EDS analysis of the SPSed-A sample shows oxygen is present in the sample. It was enough evidence that the SPSed-A sample had a huge amount of impurity that resulted in very poor densification (~5.2g/cc). In other sintered samples, it was observed that a small amount of tungsten was present. It may be contaminated by tungsten vial and tungsten balls.

6.4.2 Indentation Characteristics Analysis

The Vickers micro-indentation experiment was carried out for the investigation of nature of indentation for the SPSed alloys. It has been observed in SPSed-A alloy, the micro-hardness value continuously decreases with load (cf. fig. 6.25(a)),this demonstrates a significant ISE[217]. However, in other SPSed alloys the micro hardness value first increases with the load and then becomes constant or independent of load (cf. fig. 6.25(b-d)), this demonstrates a significant effect of RISE[209], [231]. It mostly takes place in materials where plastic deformation is predominated. The maximum Vickers micro hardness and reduced elastic modulus was observed in SPSed-C (~11 GPa) and (~206 GPa) respectively. Although the minimum micro-hardness was found in SPSed-A (~3 GPa) at 100g load. The micro hardness, Young's moduli of the present sintered alloys were found to be higher than many BMGs[49], [232]–[234]. It is observed that fine crack was appeared in the indentation impression of SPSed-C and SPSed-D alloys at 1000g of applied load while SPSed-B is free from crack up to 1000g load. The absence of crack around the indented area of SPSed-B, indicates better toughness of this sintered alloy and also suggests this alloy has more resistance to crack propagation as compared to others[189]. The nature of these cracks is Palmqvist type. The indentation fracture toughness value for SPSed-C and SPSed-D alloy is found to be 3.6 and 3.22 $MPa.m^{1/2}$ respectively at 1000g load. The indentation fracture toughness of these sintered alloys are found to be greater than those reported by Abbas et al.[170] for FeCo

based composite, Zhang et al.[233] for BMG composition. From the P-h curves of sintered alloys, it was observed that the indentation depth increases with decreasing the hardness. The maximum depth of penetration (~3.22μm) was observed in SPSed-A. A small pop-in (displacement discontinuity) event has been observed in the loading part of the P-h curve of SPSed-B and SPSed-C alloys, similar to Iqbal et al.[235] and Wang et al.[232]. Although SPSed-A and SPSed-D shows relatively smooth P-h curve. The non-uniform penetration in these SPSed alloys is due to either plastic deformation or formation of cracks[235]. The different deformation behaviour is attributed to the different microstructures of these SPSed alloys[217]. The 0.2 % offset yield strength (σ_o) was found maximum for SPSed-D alloy (~8 GPa) at 100g load. The Meyer index (n)[176], [191], [236] estimated from exponential curve fitting to the indentation diagonal d (mm) versus applied load P(Kg) from a straight line graph of Log(d) versus Log(P)[237]. Meyer's index is related to "work- hardening index" and their value lies in the range of ~ (1.6 - 2) for SPSed alloys.

Indentation experiment also provides a suitable way to measure the magnitude of deformation. The area under P-h curve, provides a measure of elastic and plastic energy components of deformation during indentation[177]. Three important parameters, (i) plastic criterion (R_w)[179], (ii) elastic-recovery (R)[120], and (iii) percentage of elastic recovery (%R)[120] were calculated from P-h plots. The value of elastic recovery ($R=h_f/h_{max}$) for SPSed alloys are in the range of (0.6-0.8), while percentage of elastic recovery (%R) found in the range of (28%-37%). The maximum elastic recovery was found correspond to SPSed-C (~37%). The indentation work done for elastic work recovered during indentation test is observed maximum for SPSed-B alloy (~70%). The H/E ratio is obtained maximum for SPSed-D (~0.055), it indicates the elastic recovery is more in this alloy. The H/ρ ratio of the sintered alloys is found to be 0.59, 1.11, 1.44, and 1.59 in SPSed-A, SPSed-B, SPSed-C and SPSed-D respectively. Owing to high level of porosity in the sample of SPSed-A, it has the lowest value of H/ρ. The H/ρ ratio in maraging steel [192] was reported to be 0.52. The H/ρ ratio of present sintered alloy was found to be ~3 times higher than maraging steel (in particular SPSed-D). The maximum specific stiffness (E/ρ) among the sintered alloys is found in SPSed-D (~29). The specific stiffness is also higher than maraging steel (~18.64)[192]. This aspect may be useful for designing engineering components for specific applications.

6.5 Conclusions

The microstructure, phase evolution, and indentation characteristics of four different alloy compositions processed through ball milling and its consolidation were studied. The following conclusions can be drawn:

(i) The morphology of ball-milled powders of sample BMP-A and BMP-B changes with milling time and at the end of milling (~100h) spherical morphology achieved. Although, in case of BMP-C and BMP-D, the faceted morphology obtained.

(ii) The of α-Fe (cI2) and $Fe_{11}Mo_6C_5$ (mC44) are retained in the ball milled powders at the end of milling (~100h). Further, 100h of ball-milled powders consolidated through SPS technique gave some new crystalline phases $Fe_{23}C_6$ (CF116) and $FeMo_2B_2$ (tP10) in addition to the above.

(iii) The high hardness and reduced Young's modulus value was observed for SPSed-C i.e. ~ 11 GPa and ~206 GPa respectively. The 0.2 % offset yield strength was found maximum for SPSed-D (~8GPa) at 100g applied load. The indentation depth was found maximum correspond to SPSed-A alloy (~3.22μm). Therefore, the minimum hardness obtained (~3GPa) correspond to it. One of the main reasons for getting poor hardness in SPSed-A is its poor densification.

(iv) The Palmqvist type of crack is observed in SPSed-C and SPSed-D alloys at 1000g applied load. The average indentation fracture toughness in these sintered alloys was obtained ~ 3.6 $MPa.m^{1/2}$ and 3.22 $MPa.m^{1/2}$ respectively. The absence of crack around the indented area of SPSed-B, indicates its better toughness and also suggest this alloy has more resistance to crack propagation as compared to others.

(v) The value of elastic recovery ($R=h_f/h_{max}$) for sintered alloys are found in the range of (0.6-0.8), while percentage of elastic recovery (%R) are in the range of (28%-37%).

(vi) The H/E value is obtained maximum for SPSed-D alloy (0.055), it indicates that elastic recovery is more in SPSed-D. The hardness to density ratio (H/ρ) and specific stiffness (E/ρ) are found to be maximum for SPSed-D alloy and they are 1.59 and ~29 respectively.